

A CONDUCTIVITY-BASED MEASUREMENT DEVICE TO
DETERMINE VOLUME FRACTION AND GAS SLIP VELOCITY FOR
MULTIPHASE FLOW

by

Mazin Saied

Submitted in partial fulfillment of the requirements
for the degree of Master of Applied Science

at

Dalhousie University
Halifax, Nova Scotia
May 2017

© Copyright by Mazin Saied, 2017

This thesis is dedicated to my parents, for their endless love, support and encouragement.

Table of Contents

List of Tables	vi
List of Figures	vii
Abstract	x
List of Abbreviations and Symbols Used	xi
Acknowledgement	xiii
Chapter 1 INTRODUCTION	1
Chapter 2 LITERATURE REVIEW	4
2.1 Conventional Test Separators	4
2.2 Compact Separation Technology	5
2.2.1 Compact Gas-Liquid Separator by LCC	6
2.2.2 Two inline Separator & Topside Gas/Liquid/ Water	6
2.3 Absorption	8
2.3.1 Nuclear Technique	8
2.3.1.1 Schlumberger Venturi X Meter	8
2.3.1.2 Roxar Multiphase Meter (MPFM)	9

2.3.2	Microwave Technique	10
2.4	Electromagnetic and Pattern Recognition Techniques	12
2.5	Conductivity Based Sensor Design	13
2.5.1	Current applications based on a different technique to detected bubbles traveling through the channel	13
2.5.2	Electrical Conductivity and Capacitance Measurement	17
2.5.2.1	Conductivity Capacitance Application	17
2.5.2.2	Wire Mesh Sensor Base on Conductivity Measurement	17
Chapter 3	EXPERIMENTAL DESIGN OF A SINGLE-POINT SENSOR	20
3.1	Methodology	21
Chapter 4	IMAGE AND ELECTRICAL ANALYSIS	24
4.1	Image-Based Bubble Velocity Determination	26
4.2	Synchronizing Bubble Width and Electrical Response	27
Chapter 5	RESULTS AND DISCUSSION	30
5.1	Bubble Velocity From Image Analysis	30
5.2	Bubble Width	31
5.3	Calculated gas hold-up	41
5.4	Bubble velocity from single-point measurement	45

Chapter 6	CONCLUSION	49
Bibliography	51
Appendix A	First Appendix	55
A.1	Bubble Width vs. Voltage Response For Small Bubbles	55
A.2	Bubble Width vs. Voltage Response For Small Bubbles	58
A.3	Bubble Velocity	62
A.4	Bubble Velocity	65

List of Tables

Table 3.1	Flow conditions for which this sensor has been validated.	23
Table 5.1	Test of a time shift and bubble velocity for distance, gas velocity, and liquid velocity.	31

List of Figures

Figure 2.1	Conventional test separator (Uleh, 2013).	5
Figure 2.2	Two inline separator (Mikkelsen et al., 2013).	7
Figure 2.3	Schlumberger venturi x meter (Uleh, 2013).	9
Figure 2.4	Roxar MPFM (Uleh, 2013).	10
Figure 2.5	Testing prototype sensor by microwave test in the lab (Wylie et al., 2006).	12
Figure 2.6	Droplet detection scheme (Elbuken et al., 2011)	14
Figure 2.7	Schematic diagrams of (a) sample detection and (b) fluorescence-activated sorting in conventional low cytometry. In (a) cells are injected into the core of a sheath flow and are confined to a narrow, single-file stream via hydrodynamic focusing (Huh et al., 2005). . .	16
Figure 2.8	Wire mesh sensor based on capacitance (Hampel et al., 2009). . . .	18
Figure 2.9	Wire mesh sensor based on conductivity (Demori et al., 2010, Da Silva et al., 2007).	19
Figure 3.1	Schematic of the conductive sensor	21
Figure 3.2	Photos of the experimental setup in the lab.	22
Figure 4.1	A (Raw), B (background corrected) and C (binary) bubble image correction using Image <i>J</i> software aA case (2).	25

Figure 4.2	Excerpt of image-based bubble the before (dashed black) and at the probe (orange) for case (5) before the shifting.	25
Figure 4.3	Excerpt of Image-based bubble width before (dashed black) and at the probe (orange) for case (5) after shifting.	26
Figure 4.4	Aligned bubble width before and at probe for case (6).	26
Figure 4.5	Flow conditions and Image measurement locations for case 6 (top), case 5 (middle) and case 1 (bottom).	27
Figure 4.6	Error minimization as a function of the electrical time shift for case (5).	28
Figure 4.7	Bubble width vs electrical signal at case following alignment (5). . .	28
Figure 5.1	Electrical signal response during initial introduction of bubbles for case (5).	32
Figure 5.2	V_{max} Determined for each of the flow conditions tested.	32
Figure 5.3	Resistance model used within this system.	33
Figure 5.4	Illustration of bubble path length and open area for conduction as bubbles travel through the sensor.	34
Figure 5.5	Electrical signal response, ΔV , for one bubble traversing the probe. .	35
Figure 5.6	Provides an example of the bubble width vs $(1 - V / V_{max})$ observed following synchronization of the image data and electrical measurements.	37
Figure 5.7	Average bubble width vs electrical response for case 1 (top) to case 7 (bottom), and error bars represent a single standard deviation. . .	39

Figure 5.8	Overlay of average bubble width for case 1 (top) to case 7 (bottom).	40
Figure 5.9	Relationship between W/D and gas fraction estimated from Eq.s 5.7 and 5.8 for circular and stratified flow.	42
Figure 5.10	Gas fraction for three cases from the image, electrical and flow-based data for increasing values of t_{sample}	43
Figure 5.11	Gas fraction from the electrical data for all conditions.	44
Figure 5.12	Gas fraction from the electrical data vs calculated gas fraction.	45
Figure 5.13	Predicted velocity (m/s) vs dimensionless bubble width for case 3.	47
Figure 5.14	Predicted bubble velocity derived from electrical data (Eq. 10) vs. image-based bubble velocities for each of the cases tested.	48

Abstract

Multiphase flow metering is needed in the oil and gas industry for well-monitoring, gas fraction, oil cut, and water cut and tracking of solid content are the key parameters regarding well measurement. The two-phase flow of gas and liquid is regularly used in the design and operation of heat exchangers and mass transfer equipment for several industries and power plants. For multiphase flow involving fluids with different electrical properties, electrical conductivity could be used for visualization of flow regimes and flow metering.

This work explores the use of a low-cost sensor to study the dynamic response of conductivity for slug flow. A conductive sensor consisting of a voltage source and a measurement device was used to determine the conductivity between two electrical probes inserted into the flow at a spacing of 3.752 mm. The velocity and shape of the bubble entered the sensor was measured using high-speed photography and was used to correlate the electrical signal response to bubble characteristics. The current research is exploring the feasibility of using the electrical response of conductive fluids for reconstructing the conductive path length, from which bubble shape and velocity can be determined within a given confining geometry.

List of Abbreviations and Symbols Used

GOR	gas/oil ratio
LCC	normalized mode length
MPPT	Multiphase Power and Processing Technology
CTOP	Compact Topside Gas-liquid-liquid
RXM	Roxar Multiphase meter
RSMM	Roxar subsea multiphase meter
MPFM	Multi phase flow meter
HFSS	High-Frequency Structure Simulator
U_L	Liquid velocity (m/s)
ω_o	Resistivity
A	Normalized area (mm^2)
U_B	Bubble velocity (m/s)
U_{Bimage}	Bubble velocity from image data (m/s)
U_{Bmode}	Bubble velocity from the correlation (m/s)
U_g	Gas velocity (m/s)
w	Bubble width (mm)
V	Voltage (v)
v_{max}	Maximum voltage
α	Gas fraction
Δv	Change of the conductivity
κ	Electrical conductivity
μ	Viscosity of the fluids
Q_L	Liquid flow rate ml/min
Q_G	Gas flow rate (Scm)
L	Channel length (mm)
t	time (s)
dt	derivative time (s)
D	Diameter (mm)
A_{fluid}	Area available for conduction (mm^2)

L_{fluid} Path length (mm)

R_{sensor} Resistance of the fluid in the sensor (Ω)

Acknowledgement

First and foremost, I wish to thank Allah for everything given to me. I would also like to express my sincere gratitude to my supervisor, Dr. Adam, for his continuous support of my Master's degree. studies and related research, and for his patience, motivation, and immense knowledge. I appreciate all his contributions of time, ideas, and funding during my degree. His guidance helped me throughout the research and writing of this thesis, and his hard questions gave me incentive to broaden my research from various perspectives.

My thanks also go the best love I have my wife Wafa she spent many sleepless nights with me and was always my support in moments when there was no one to answer my queries.

A special thanks to my mother, sisters, and brothers for supporting me emotionally and spiritually throughout the writing of this thesis and my life in general. I cannot thank you enough for encouraging me, and I know that your prayers helped sustain me throughout this journey. I never, ever forget my beloved daughter Salma, and my beloved sons, Kenan. I would like to express my thanks for being such good girls and boys and always cheering me up.

Chapter 1

INTRODUCTION

Well monitoring is a regulatory requirement for oil producers, and is crucial for improving the production of formation fluids through accurate estimates of the total flow rate, water cut, oil cut, pressure and temperature (Leffler et al., 2011, Uleh, 2013). While these parameters can be determined by using a traditional separator, this is typically not feasible for every well on a continuous basis. Test separators cost approximately USD 500,000 to 1,200,000, depending on the size and pressure. These cost estimates are for onshore and topside applications, respectively, and represent hardware costs only ((Falcone et al., 2009). As valuable finds in mature fields (e.g., the North Sea) are reduced, companies increasingly face challenges in developing smaller areas that they previously may not have considered worth developing. Cost-efficient solutions are continuously being explored, including the use of shared transportation pipelines, shared production facilities, metering systems and the development of automated platforms. Multiphase flow meters are one solution to provide rapid monitoring of wells, yielding information on the total flow and relative gas and water holdup (or cuts). This thesis was designed with the intention of exploring and better understanding multiphase flow metering technology applicable to the oil and gas industry.

Multiphase flow metering (MPFM) is defined as the measurement of flow rates in each phase of a multiphase flow. Multiphase flow is a fluid flow consisting of more than one physically distinct phase (Goriely et al., 2015) and has enormous potential for various applications, such as power generation, crude oil extraction and process engineering. In the

petroleum industry, multiphase flow describes hydrocarbon gas and hydrocarbon liquid (condensate or oil) moving simultaneously through the reservoir and transporting pipeline facilities (flow line, trunk line, and riser) (Hall et al., 2007) . Based on these definitions, a multiphase flow meter is a traditional separator of two or three phases, followed by independent metering for each distinct phase. The term ‘multiphase flow metering’ appeared after the establishment of separators for industrial applications, with MPFM being conceived as the non-intrusive measurement of the simultaneous flow of two or more phases, without the need for separation (Falcone et al., 2009). New multiphase flow sampling tools serving in the field provide operators with high efficiency and accuracy when monitoring heavy oil flow in pipelines (Corona et al., 2016). The idea behind in-line sampling is to reduce the cost of expensive electronic devices that make well monitoring one of the most challenging processes facing operators in the industry. Most multiphase flow metering devices have significant drawbacks related to flow rate accuracy and a lack of representative fluid samples (Liu and Liu, 2007, Liang et al., 2015). The complexity of heavy oil production makes the monitoring process difficult, requiring proper equipment.

Over the past decade, conductivity and capacitance sensors have played a significant role in the study of gas-liquid multiphase flow phenomena in the oil and gas industries. The most current sensor technology addresses steam-water flows at high pressures and temperatures, and the measurement of non-conductive liquids using an electrical conductivity and capacitance measuring scheme (Figueiredo et al., 2016). For example, wire-mesh sensor multiphase flow imaging devices can investigate the flow in different regimes at high spatial and temporal resolutions (Corona et al., 2016). One disadvantage of this device is that the wires impact the flow profile, affecting the second point of measurement when determining bubble velocity.

The main objective of this thesis was to design and validate a conductivity-based system for a mini-fluidic channel capable of measuring gas holdup, and to explore its use in correlating

the bubble velocity from a single point measurement. The following chapters of this thesis are structured as follows.

- Chapters 2 reviews technologies used to meter multiphase flow and introduces conductivity and capacitance measurement techniques, providing detail about the fundamental methodology, limitations and advantages of these systems.
- Chapters 3 and 4 provide an overview of the physical system used in this work, and the methodology applied to quantify the data obtained from image analysis.
- Chapter 5 summarizes the results and discusses the application of this sensor to an air-water system, and Chapter 6 presents the conclusion.

Chapter 2

LITERATURE REVIEW

This chapter provides an overview of current multiphase flow metering techniques available in industry, ranging in complexity from conventional test separators (representing the separate and measure strategy) to exotic separators and new imaging approaches.

2.1 Conventional Test Separators

A common separator, as illustrated in Fig. 2.1, involves three principles for realizing physical separation: momentum, gravity settling, and coalescing. In a conventional separator, multiphase mixtures are introduced in a large volume, where they are given time to separate based on their difference in density. Each of the exiting streams in these separators can then be metered to determine the relative flow rate of each within the inlet stream. These systems work well only if separation is achieved within the volume; otherwise, the metered streams will not represent pure component flow rates. A challenge with these separators in heavy oil metering is that the density of heavy oil may be comparable to or heavier than water, thus, during production the heavy phase may change. This can require the use of density modifying solvents, or heating to assist in separation, in order to ensure that the organic phase is lighter than the aqueous phase.

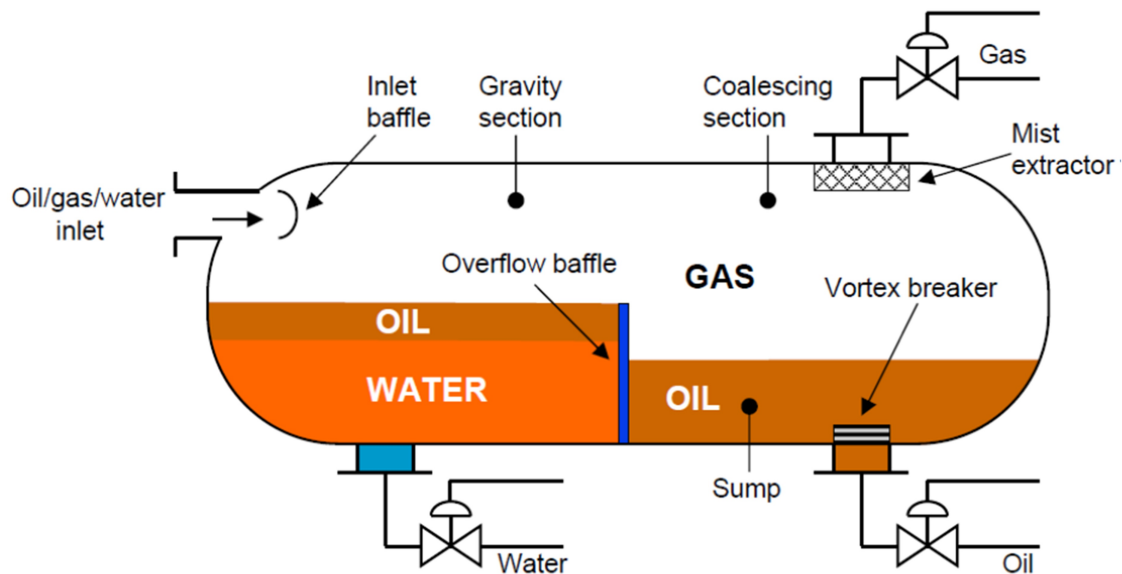


Figure 2.1: Conventional test separator (Uleh, 2013).

The performance of the separator is determined by the retention time required for gravity separation to occur. In typical commercial separators, this process occurs within one to three minutes, depending on factors such as the size of the design, the flux of fluids, the gas/oil ratio (GOR), and the oil/water ratio. The oil output separation from the first stage contains about 1 to 3% water and up to 0.5% gas.

2.2 Compact Separation Technology

There are several applications for compact separation systems, including the compact gas-liquid separator by LCC, the compact topside gas/liquid/water processing plant, and the two-phase inline gas/liquid separator. These are discussed below.

2.2.1 Compact Gas-Liquid Separator by LCC

The compact gas liquid separator by LCC is designed as a meter to measure the volumetric flow rate of the gas phase in the wet gas stream (Lessard, 2014). In the LCC design, gas passes from the top of the separator, with the separated liquid on the drum wall spinning off and continuing along the outer edge to the drain. In a modified model produced by IRIS, a rotor can be incorporated to gather liquids on the outer wall while a swirl inlet generator controls the flow to the separation point at the rotor (Prescott et al., 2016). The rotating flow at the rotor serves to enhance the force of the liquid toward the outer wall. Dry gas is separated from the center, while the liquid is separated from the spin drum wall and goes toward the separator drain. During measurement, the gas flow rate in wet gas conditions could be inferred by measuring the rotor speed. At liquid-to-gas ratios of $\leq 3\%$, the rotor speed exhibits low sensitivity (Uleh, 2013) . The liquid flow rate and the gas flow rate estimates are typically within $\pm 5\%$ of actual dry gas conditions. At higher liquid loadings, the increased fluid drag led to reduced rotor speed, whereas at a constant gas flow rate the reduction in rotor speed was proportional to the liquid flow rate. The most challenging aspects of a conventional test separator (LCC) is the cost, weight, and space requirements.

2.2.2 Two inline Separator & Topside Gas/Liquid/ Water

Multiple researchers (Kato et al., 2012, Hannisdal et al., 2012) have shown that for gas/liquid separation, highly efficient compact technologies such as inline de-liquidizers (IDEL) are used for disposal of liquid from a gas stream and inline degassers (ID) for disposal of gas from a liquid flow. Both technologies create a spin on the arriving stream, leading to the formation of a gas core enclosed by a liquid film in the separation section downstream from the swirl, as shown in Fig. 2.2. The compact topside gas-liquid-liquid approach is meant for hydro solutions. These technologies are designed to deal with future

facilities, to minimize the footprint area and weight, and to address physical conditions such as pressure, temperature, viscosity and flow rate (Kristiansen et al., 2016). The disadvantages of the compact topside separator and the two-phase inline approach are reliability and availability assessments, as the concept of compact topside gas-liquid-liquid (CTOP) separation is not based on the regulations for the design and sizing of separators (Kato et al., 2012). Unlike the situation for conventional designs, well-established design practice and performance data are not available, so it is difficult to reference extensive operating experience. For this reason, the assessment is based on basic reliability principle conditions.

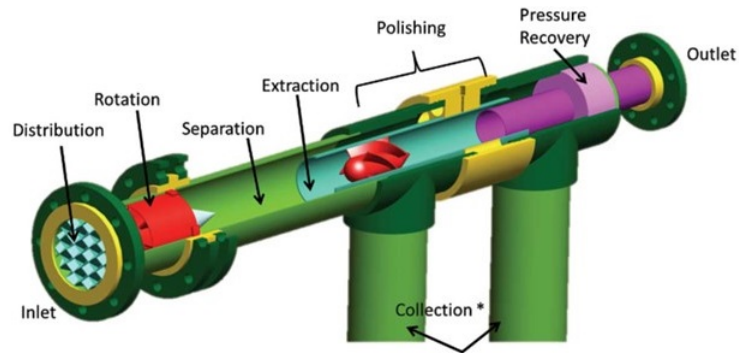


Figure 2.2: Two inline separator (Mikkelsen et al., 2013).

This might result in high pressure or a slug in the stream, leading to vibrations or strong internal forces and instrument failure. Another type of failure is caused by initial debilitation, leading to degraded performance over time that may ultimately result in critical failure. Although inline and compact technology has been in operation for some time, there are yet few reliable data for reliability assessments. Therefore, a major current challenge is achieving reliability assessments for inline compact systems.

2.3 Absorption

2.3.1 Nuclear Technique

Nuclear technology has developed in the oil and gas industry to focus on phase volume fractions in multiphase flows, due to the high thermal stability and reliability. Various nuclear approaches have been attempted in multiphase flow meters, including the use Cae-sium 137, Barium 133 and Americium 241. In addition, several methods involve radiation using gamma rays, X-rays or neutrons, with partially reduction of the radiation by the flow (Fischer et al., 2008, Johansen, 2015). Information about local density or phase distribution can be obtained by measuring the attenuation of radiation through the flow, or by triangulating the locations of radiation sources within the flow (Roshani et al., 2015) Single-energy and dual-energy are two types of gamma ray attenuation used in multiphase monitoring (Roshani et al., 2014). Although accurate, this method of measurement presents the chal-lenge of handling radioactive sources and requires carefully implemented procedures and extensive approval for use (in accordance with transportation, safety, health and environ-mental regulations) (Da Silva et al., 2007, Shamsa and Lines, 2015). Examples of com-mercially developed nuclear techniques are the Venturi X meter and the Roxar multiphase meter (RXM).

2.3.1.1 Schlumberger Venturi X Meter

Schlumberger has developed a Venturi X meter based on a Venturi measurement and a dual-energy gamma ray absorption measurement over the Venturi throat (Lessard, 2014). The meter is installed without mixing vertically with the upward flow upstream, and in the vertical section, a blind tee is recommended to improve mixing Fig. (2.3). The radioactive source for topside and onshore applications is a Gd-153 source that has energy levels of

41.5 and 97.4 keV. These two energy levels are used in the dual-energy gamma-ray absorption concept for composition measurement.

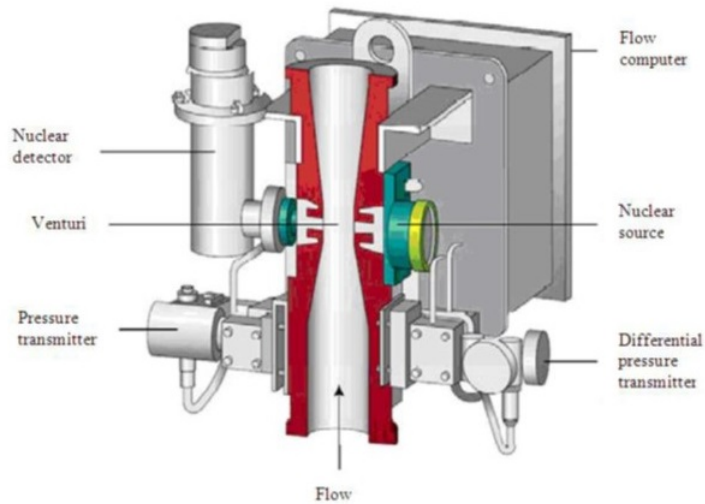


Figure 2.3: Schlumberger venturi x meter (Uleh, 2013).

2.3.1.2 Roxar Multiphase Meter (MPFM)

Roxar has developed a new technique for measuring radioactive isotopes for multiphase monitoring (Johansen, 2015). A binary velocity methodology is used, with determined phase fractions based on conductivity and capacitance measurements, combined with a single-energy gamma densitometer, cross-correlation, and Venturi section to determine the flow rates of each stage. Gamma radiation attenuation techniques are used for a mixture of two-phase fractions based on a single-energy gamma source or for three-phase mixtures using a dual-energy gamma source (Busaidi et al., 2003). The intensity of the gamma beam decays exponentially as it passes through matter flowing in through the measurement pipe section. The attenuation of the gamma ray depends upon the different densities of the materials. A material with a high density will attenuate the electromagnetic radiation more than one with lower density. If the gamma source employed has two distinct energy levels, this property can be exploited to determine the volumetric fractions of oil. The atomic

attenuation coefficients of a three-phase mixture of oil and gas depends not only upon the densities of fluids but also on the energy of the gamma rays.

The Roxar subsea multiphase meter (RSMM), shown in Fig. 2.4, is a compressed state-of-the-art meter which provides real-time accurate measurements of hydrocarbon flow rates and water production.

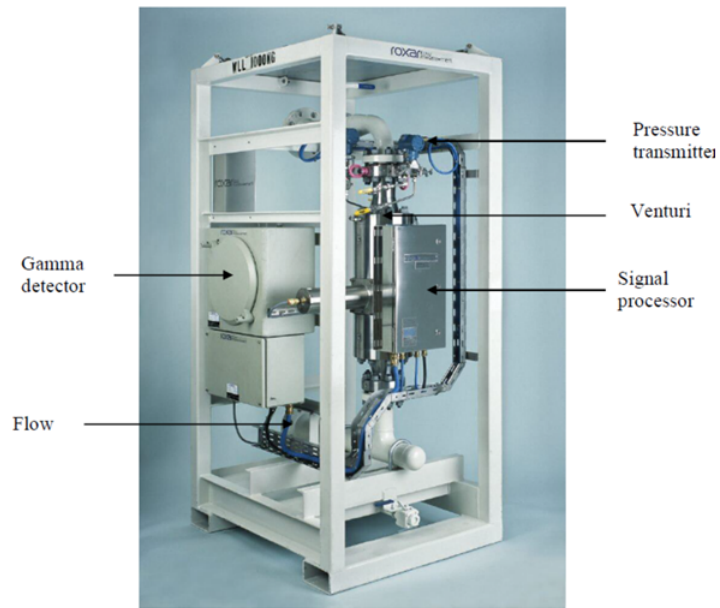


Figure 2.4: Roxar MPFM (Uleh, 2013).

2.3.2 Microwave Technique

Microwave sensors are based on the differentiation of permittivity between water and oil in the liquid phase of a multiphase flow (Nehring et al., 2014). Water and oil have distinctly different dielectric constants and conductivity that allow a microwave sensor to determine the moisture content of a water-oil mixture. Several types of microwave sensor have been developed, and more are underway. Many of the concepts and methodologies are known, although there are some new principles and techniques (Aslam and Tang, 2014). The challenge of these techniques is that the method response depends upon the flow configuration

(i.e., is geometrically dependent). Because two-phase flow has substantial variation in impedance, this method can be affected by the continuous phase and may perform poorly in the inversion region. Microwave sensors that utilize electromagnetic fields and devices operate internally at frequencies from ~ 300 MHz up to the terahertz range. Microwave devices can be found in different classes, such as transmitter-receiver systems, passive detectors (radiometers) and resonator sensors.

The basic design of a microwave sensor was developed at the Liverpool John Moores University. The original sensor used a 10 W signal over a range of frequencies and detected resonant peaks occurring within the cylindrical cavity of the sensor. These resonant frequencies shift if the permittivity of the multiphase flow changes. A modern version of the sensor for a 102 mm (4-inch) diameter pipe was constructed, and trials connected to the test loop were performed at the National Engineering Laboratories (NEL) in the UK, with stratified and annular flow regimes (Al-Kizwini et al., 2013). Microwave resonators are designed as a unit of the transmission line with open or shorted ends. This means the resonant stub is a length of transmission line or waveguide that is connected at one end only. The names of the resonators reflect the type of transmission line used (e.g., micro strip, strip line, plotline, coaxial or cavity models). When the resonator functions as a sensor, the object to be measured is brought into contact with at least part of the electromagnetic field in the resonator. Therefore, the resonant frequency and the quality factor will change in relation to the permittivity of the object. Due to the large variety of possible structures, sensors can be designed for the measurement of almost any kind of object. The major advantage of microwave sensors is their capability of measuring non-destructively and without contact from a short distance, using penetrating waves that do not cause health risks to personnel. Drawbacks include the high degree of specialization and the concurrent existence of several variables affecting the microwave measurement (moisture, structure, temperature, density, etc.) in material measurements (Al-Kizwini et al., 2013). Basically,

the transmission sensor consists of two horn antennas: A transmitter and a receiver. The object to be measured is placed between the antennas in such a way that the microwaves pass through the object. Either the attenuation, the phase shift, or the resonant frequencies are measured.

Figure 2.7 shows a microwave technology prototype in a laboratory. The model consists of the cavity section with the receiver and transmitter antennas, and two narrower sections on either side to represent the pipeline entering and leaving the sensor. A 10 dBm (10 mW) output from the spectrum analyzer, at frequencies ranging from 100 MHz to 1 GHz, was fed into the transmitter and was detected by the receiver antenna. The pipeline section is gradually filled with water and oil, representing a stratified regime (Prescott et al., 2016).

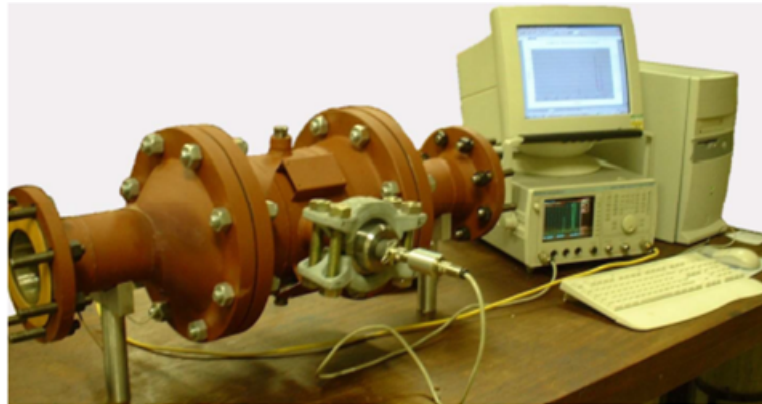


Figure 2.5: Testing prototype sensor by microwave test in the lab (Wylie et al., 2006).

2.4 Electromagnetic and Pattern Recognition Techniques

These techniques are focused on flow properties, where investigation of the conductance and capacitance of the fluids traveling through an electrical field may permit measurement of the flow rate and the gas fraction distribution (Gao et al., 2016). There are different applications that focus on electrical techniques, such as conductivity and capacitance measurement techniques (Strazza et al., 2011).

2.5 Conductivity Based Sensor Design

2.5.1 Current applications based on a different technique to detected bubbles traveling through the channel

One of the dominant parameters of gas-liquid two-phase flow in industrial equipment is the measured gas fraction. Various techniques have been used to investigate gas holdup and to calculate bubble velocity by using DC voltage, AC voltage, microwave technology, ultrasound, and fiber optics. All these methods are based on fluid property concepts. Moreover, each of these techniques has advantages and disadvantages, which may make the approach less useful or difficult to modify. For conductivity based on DC voltage, the current is applied to a gas-liquid two-phase flow through electrodes that are inserted into the surface of the channel. Another electrode perpendicular to the applied voltage is used to measure the voltage drop in the system. Conductivity based on DC voltage can provide fast response times, however, it tends to cause corrosion in the system because of the continuous voltage during operation.

(Hampel et al., 2009) developed a wire mesh sensor to investigate fluid flows with a gas distribution. In the case of electrically conducting and non-conducting phases (for example, air and water), the resulting conductivity measurements are an indication of the phase present at each crossing point. Hence, the sensor can determine instantaneous void fraction distributions over the pipe cross-section.

(Uesawa et al., 2013, Fukano, 1998) have provided an approach to evaluate the gas holdup for three-dimensional flow containing microbubbles, by using a constant electric current method. A more accurate gas fraction estimation is achieved, based on Maxwell's theory and the polarization method.

Capacitance measurement based on AC voltage focuses on capacitance variations in the fluid, and can use an insulation fluid. The capacitance phenomenon is related to the electric field between the two plates of the capacitor (Terzic et al., 2012). Increasing the distance between the two conducting plates decreases the electric field between the plates.

((Strazza et al., 2011) investigated gas holdup, where the bubble flow behavior was monitored in a liquid batch bubble column subject to artificial dual capacitance. A wire mesh sensor was used to provide preliminary results, approaching the measurement of a local void fraction. The effect of vessel motion on bubbly flow was emulated by using a swell simulator to expose flow structure changes emerging in the bubble columns. This approach is relevant to offshore floating applications. Other systems such as fiber optics, microwave sensors, ultrasound and flow cytometry have been used to detect bubbles traveling through the sensor.

(Elbuken et al., 2011) studied the use of a single pair of electrodes to detect the presence of a droplet. The size and speed of the droplet were determined by using an interdigital finger design. An analytical model was developed to predict the detection signal and to guide the experiment. The cost-effective sensor design uses changes in capacitance to determine droplet presence, size and speed, as shown in Fig. 2.6.

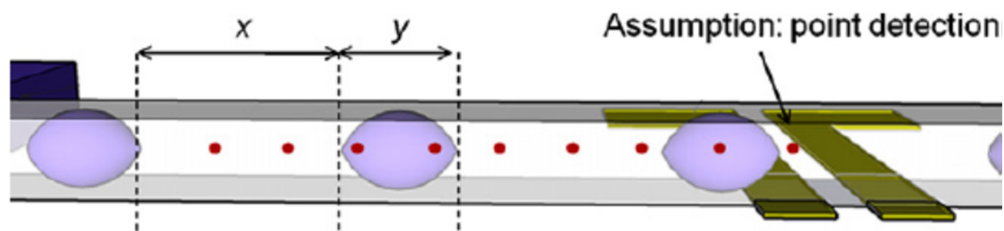


Figure 2.6: Droplet detection scheme (Elbuken et al., 2011)

Other techniques perform detection based on signal attenuation. (Wu et al., 2016) showed that an electromagnetic wave (or ultrasonic) signal generator sends a signal of a specific

power at a set frequency. The transmitted electromagnetic wave signal is received by the receiver after passing through the two-phase flow. Due to the differing attenuation of the electromagnetic wave signal as it passes through the gas phase and the liquid phase, with the aid of computer software, the flow pattern, volume and velocity of the two-phase flow can be obtained by using statistics concerning the amount and time of the electromagnetic wave signal attenuation.

(Gang et al., 2016) developed a microbubble-based FPI for high-frequency ultrasound detection. The detecting head is compact, with a diameter of 120 μm , and the fabricating process is simple and cost-efficient, requiring only a fusion splicer. The experimental results show that the proposed sensor exhibits high sensitivity to both continuous and pulsed ultrasound at 1 MHz. This approach has the advantages of good direction, strong penetration, and a long propagation distance in liquid and solid media. The disadvantages are that the results are easily affected by the ambient electromagnetic field, spatial resolution is limited due to the large size, and there is weak multiplexing ability (Gang et al., 2016, Shuyu and Shuaijun, 2011).

Flow cytometry can be used to investigate the physical and chemical characteristics of particles in a fluid as it passes through at least one laser beam Fig. 2.7. Cell components are labeled fluorescently and then excited by a laser to produce light at varying wavelengths. This technique can be used to track light time vs dark time, and the relative time of bubbles vs liquid, to estimate the gas holdup. However, the complexity of the calculations required to determine bubble velocity limit the usefulness of the flow cytometry method for estimating velocity (Huh et al., 2005).

Because these techniques are costly to implement and mechanically complex, they are not well adapted for estimating gas holdup and calculating the bubble velocity.

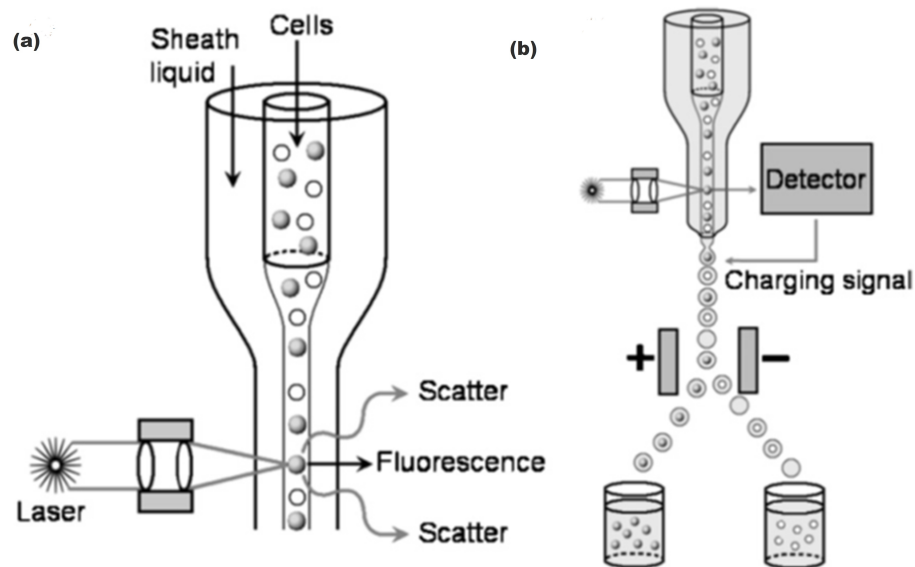


Figure 2.7: Schematic diagrams of (a) sample detection and (b) fluorescence-activated sorting in conventional flow cytometry. In (a) cells are injected into the core of a sheath flow and are confined to a narrow, single-file stream via hydrodynamic focusing (Huh et al., 2005).

(Wu et al., 2016) investigated a bubble detection method based on light scattering imaging, where a laser beam generated by a laser irradiates the water. When the water contains bubbles, the incoming beam deviates from its original orientation and scatters in various directions. Because laser beams encountering different forms of bubbles scatter in different directions, the light scattered in a specific direction can be imaged by using a charge coupled device (CCD) camera, and via image processing and theoretical calculations, the volume, velocities, and distribution of the bubbles can be obtained .

In summary, this section has shown that electrical systems provide potential benefits, and can yield shape information based on electrical responses and easily processed electrical signals. With regard to the content of the electrical signal, there are three main approaches:

A microwave approach based on electromagnetic field variation, an AC system which focuses on capacitance changes in the fluid, and a DC system with conductivity-based measurements. The system which uses DC voltage is relatively simple to implement, with the potential to provide fast response times, but requires consideration of corrosion due to the continuous applied voltage. In this research, the aim is to validate techniques for investigating the gas holdup and bubble velocity using conductivity as a basis for measurement.

2.5.2 Electrical Conductivity and Capacitance Measurement

The principle of electrical conductivity and capacitance measurement is the determination of the change in voltage drop between the probes in accordance with Ohm's Law (Schroder, 2006).

2.5.2.1 Conductivity Capacitance Application

These techniques are important and developed rapidly to meet the demands of the market and the oil and gas industry (Lim et al., 2016). An example is a wire mesh sensor, which will be discussed briefly in the next section.

2.5.2.2 Wire Mesh Sensor Base on Conductivity Measurement

Wire mesh sensors have been developed to investigate fluid flow with gas distribution (Lim et al., 2016, Tan et al., 2016). The flow meter is based on the measurement of the local instantaneous conductivity of the two-phase mixture (Demori et al., 2010, Hampel et al., 2009). The time resolution of the sensor is around 1024 Hz. The sensor is a hybrid solution between intrusive local measurement of the phase fraction and cross-sectional tomographic imaging. The model consists of two planes of grids, each of which has 16 electrodes, resulting in 16×16 fine points. These points are equally distributed over the cross-section,

and the planes of parallel wires are positioned perpendicular to one other, thus forming a grid of electrodes, as shown in Fig. 2.6.

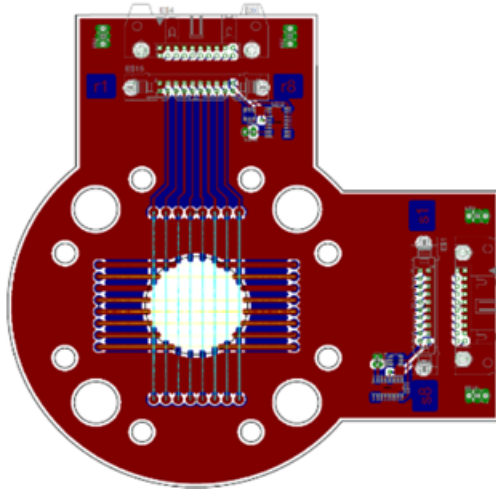


Figure 2.8: Wire mesh sensor based on capacitance (Hampel et al., 2009).

The advanced signal acquisition circuitry guarantees the suppression of crosstalk between selected and non-selected electrodes. In this case, the highest spatial resolution of the model is achieved, with one plane of electrodes serving as current transmitter electrodes and the other plane receiving the current. The distance of a few millimeters between electrodes permits conductivity measurement at the crossing points of the electrodes. Two-phase flow is studied, consisting of electrically conducting and non-conducting phases (for example, air and water). The resulting conductivity measurements are an indication of the phase present at each crossing point. Hence, the sensor can determine instantaneous void fraction distributions over the pipe cross-section.

(Crabtree, 2009, Lessard, 2014) describe the measuring principle, which is a multiplexed excitation-measuring scheme. One plane of wires works as transmitters and the other as receivers. Fig. 2.7 shows a block diagram of the configuration of the electronics in a conductivity wire mesh sensor. The transmitter sensor wires are activated by supplying

them with bipolar voltage pulses in sequential order via S1–S4 switches. The non-activated electrodes are connected to the ground. At the receiver wire, the current resulting from the activated transmitter wire is a measure of the conductivity of the fluid in the corresponding control volume close to the crossing point of the two wires. This measurement is repeated for the rest of wires in the sensor (Hampel et al., 2009).

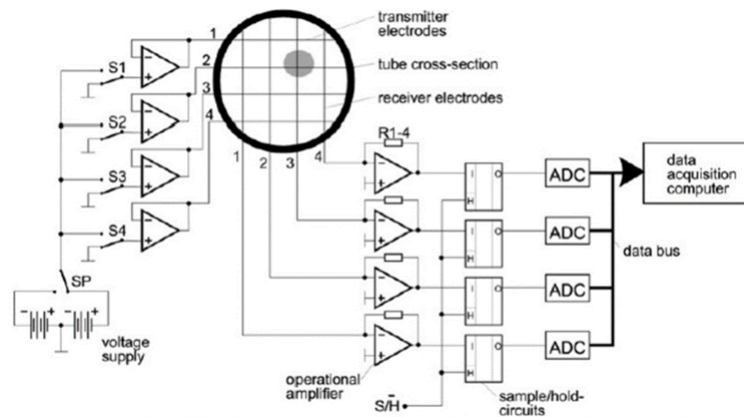


Figure 2.9: Wire mesh sensor based on conductivity (Demori et al., 2010, Da Silva et al., 2007).

Each of the measured signals reflects the structure of the flow in the associated sub-region. In this way, each crossing point acts as a local phase indicator. Moreover, all data obtained from the sensors represent the phase distribution over the cross-section. The technology of wire-mesh sensors has significantly improved regarding increased bubble size, frame rate resolution, and gas-phase velocity measurement.

Chapter 3

EXPERIMENTAL DESIGN OF A SINGLE-POINT SENSOR

Electrical conductivity measurement is one of several metering techniques in the oil and gas field that involves fraction phase distribution. It relies on measurements of variations in electrical properties of the flow to provide an image of the pipeline contents for measuring gas and liquid volume fractions in a multi-phase flow. By depending on the properties of the flow, the instrumentation may determine the resistance, capacitance or complex impedance of the flow to locate the gas and liquid phases.

This section investigates several options for multiphase meter development, based on the electrical conductivity of fluids flowing through a horizontal pipe. The focus is on the key challenges of multiphase flow metering in the oil and gas industry, with the calculation of gas distribution and slip gas velocity for different flow regimes. Because the flow characteristics in small-scale pipes, such as mini-fluid channels, make the parameter measurement more difficult than in regular pipes (Ji et al., 2014), which parameter measurement techniques can be applied and how to implement them in micro-pipe two-phase flow research becomes a critical problem (Schneider et al., 2012), Several tests have been carried out to find a simple way to construct a sensor based on conductivity measurement. The design development varies according to the different methodologies involved; however, the concept is the same across all techniques. In this case, LabVIEW software is used. A sub vi consists of an analog input DAQ assistance card (9220) to acquire voltage and to connect to the breadboard circuit. As well, the circuit is connected to an analog output DAQ assistance

Card (9269) to generate a DC voltage potential. Evaluating voltage signals generated via DAQ assistance permits measurement of the electrical conductivity of the space between crossing points for different fluids. This methodology facilitates an extensive investigation of several options for the conductivity measurement. The fluids used in the experiments were air as the gas phase and tap water as the liquid phase.

3.1 Methodology

The measurements were carried out by using a nonconductive acrylic square rod to allow for visual observation of the flow patterns before and after the measurement point. A circular channel with a 3.75 mm inner diameter was drilled through the geometric design (Fig. 3.1). Another channel with the same diameter was also drilled on the top side, to serve as the gas injection point. Then two 14-gauge copper probes were inserted perpendicular to the channel to measure the voltage. A T-mixer was used for air-water injection to generate the 2-phase flow patterns observed. The high-speed camera was capable of measuring full-frame resolution images at 4000 f/s , while the single-point electrical sensor operated at a frequency of 100 KHz . The liquid and gas flow rates were controlled by using a calibrated metering gear pump and a gas mass flow controller (0 to 500 sccm), respectively.

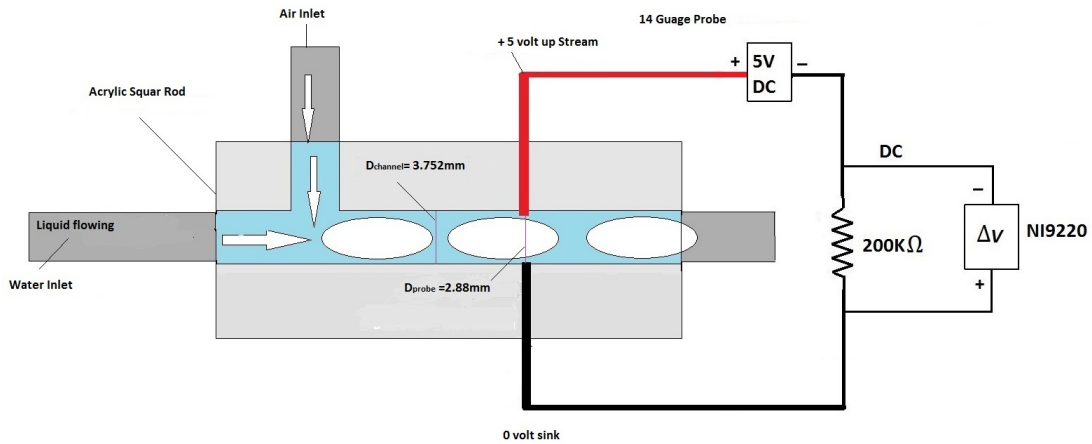


Figure 3.1: Schematic of the conductive sensor

The system was initially filled with water and the DC voltage was applied. Electrical measurement was initiated, after which the camera began recording while gas was injected into the geometry. Typical experiments lasted for 3 to 10 seconds, after which several hundred bubbles had been recorded to ensure statistical significance in the subsequent analysis. The results of the electrical measurement were recorded in an Excel file, and images were post-processed with the aid of *Image J*. For each experiment, images were background corrected, converted to binary format and analyzed to determine bubble velocity and bubble width before and at the electrical probe location. Additional details concerning the image analysis are provided in Chapter 4.

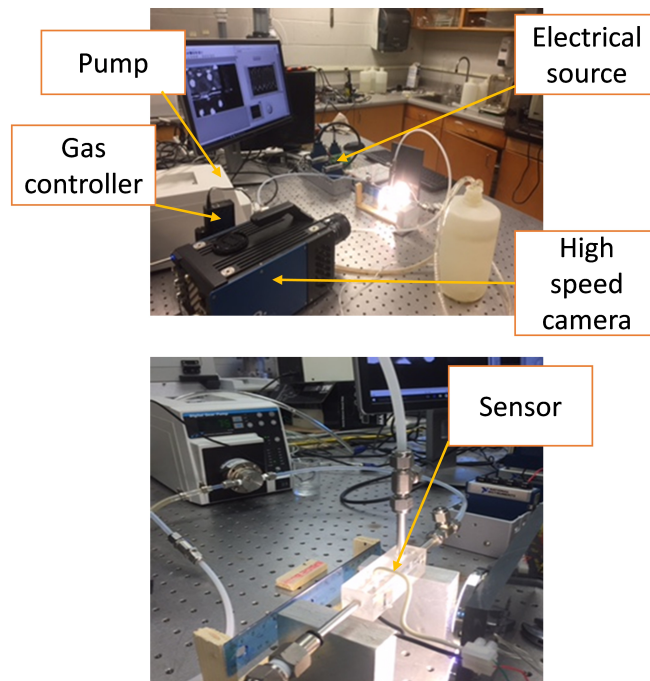
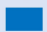



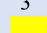











Figure 3.2: Photos of the experimental setup in the lab.

The flow rates used in this work are provided in Table 3.2. These rates were chosen at different ratios with gas holdup varying from 18 to 86% to validate the methodology over a range of potential conditions where slug flow is present. Representative pictures are provided for each condition to illustrate the nature of the flow present.

Table 3.1: Flow conditions for which this sensor has been validated.

Case	Gas flow rate (<i>Scm</i>)	Liquid flow rate (<i>ml/min</i>)	$U_B = U_L + U_G$ (<i>m/s</i>)	$\alpha \sim \frac{U_G}{U_L + U_G}$	Pictures of flow cases
1 	100	450	0.83	0.18	
2 	50	200	0.38	0.2	
3 	100	200	0.45	0.33	
4 	150	250	0.6	0.38	
5 	100	100	0.3	0.5	
6 	150	50	0.3	0.75	
7 	300	50	0.52	0.86	

Chapter 4

IMAGE AND ELECTRICAL ANALYSIS

The images collected for each flow condition were recorded at a rate of 4000 fps and saved for subsequent processing with the Image *J* software package (Schneider et al., 2012, Nanes, 2015). Each of the image sets was converted into binary format to permit rapid analysis of bubble width at the probe location and at a distance slightly upstream of the probe location, for velocity determination. Binary conversion involved background correction, level adjustment and threshold analysis. For each experimental condition, images of liquid-only flow were used as background images, which were obtained from image stacks for different conditions. The resulting 32-bit image was subjected to a consistent level adjustment (white balancing) for each experimental set. A threshold was used to create a binary image set, highlighting the bubble against the background (thresholding binary contrast enhancement) (Schneider et al., 2012). This is usually used when detecting edges, counting particles or measuring areas. Fig. 4.1 illustrate the results of the image correction process for one example case of the image analysis.

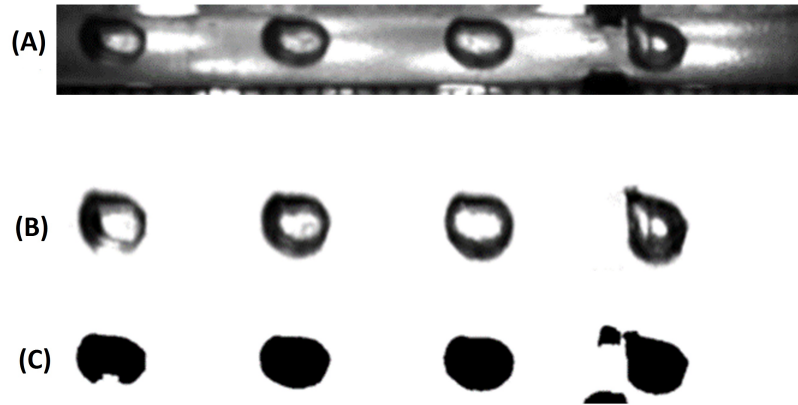


Figure 4.1: A (Raw), B (background corrected) and C (binary) bubble image correction using Image *J* software aA case (2).

The detected bubble width is depending on the threshold that used for creating binary images. As result is important to ensure consistent threshold values conversion to avoid introduction of error between experimental image sets. The bubble width was measured at two points for each of the images collected, through integration of the binary distribution across a known line segment length (Fig. 4.2).

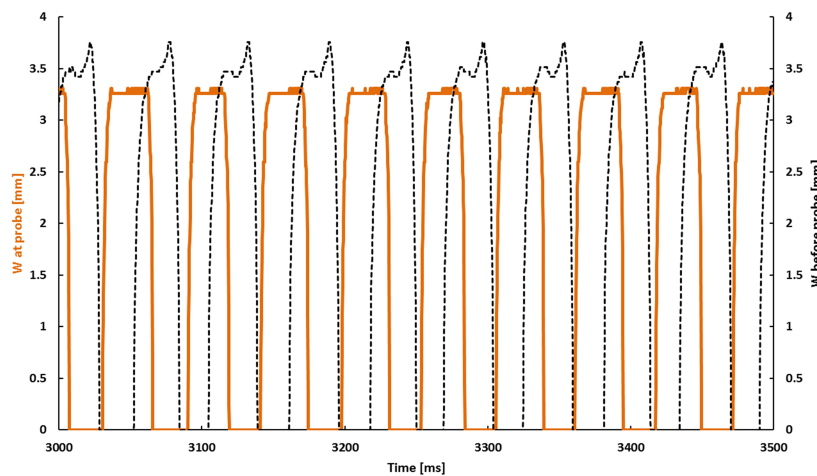


Figure 4.2: Excerpt of image-based bubble the before (dashed black) and at the probe (orange) for case (5) before the shifting.

4.1 Image-Based Bubble Velocity Determination

The next step was to investigate the phase shift by calculating the time shift required to synchronize the bubble widths before and at the probe. By aligning the two width vs time signals (Figs. 4.3 and 4.4), the time needed for the bubble to travel between the two measurement locations (Fig. 4.5) was determined, from which an accurate bubble velocity could be estimated.

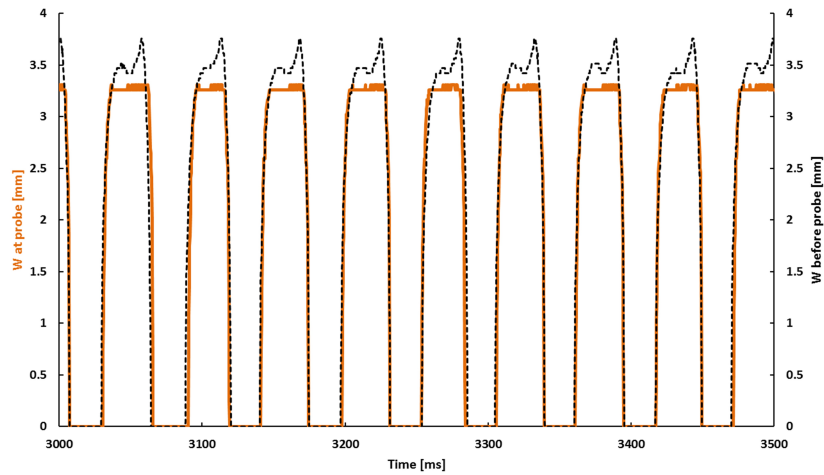


Figure 4.3: Excerpt of Image-based bubble width before (dashed black) and at the probe (orange) for case (5) after shifting.

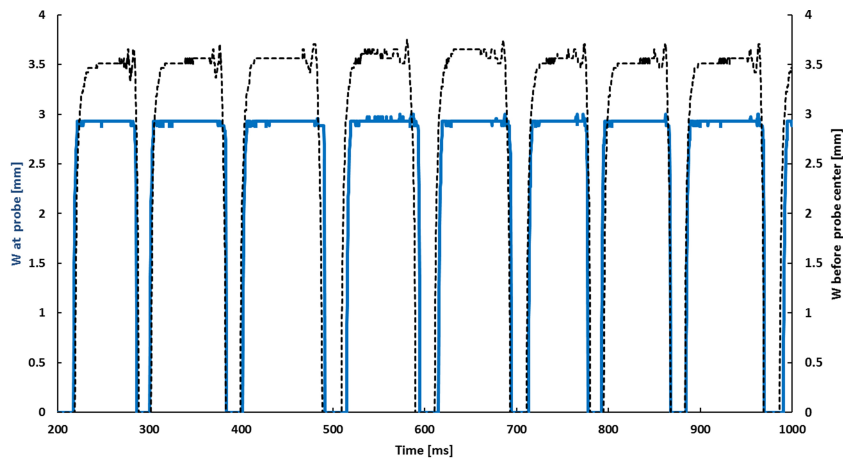


Figure 4.4: Aligned bubble width before and at probe for case (6).

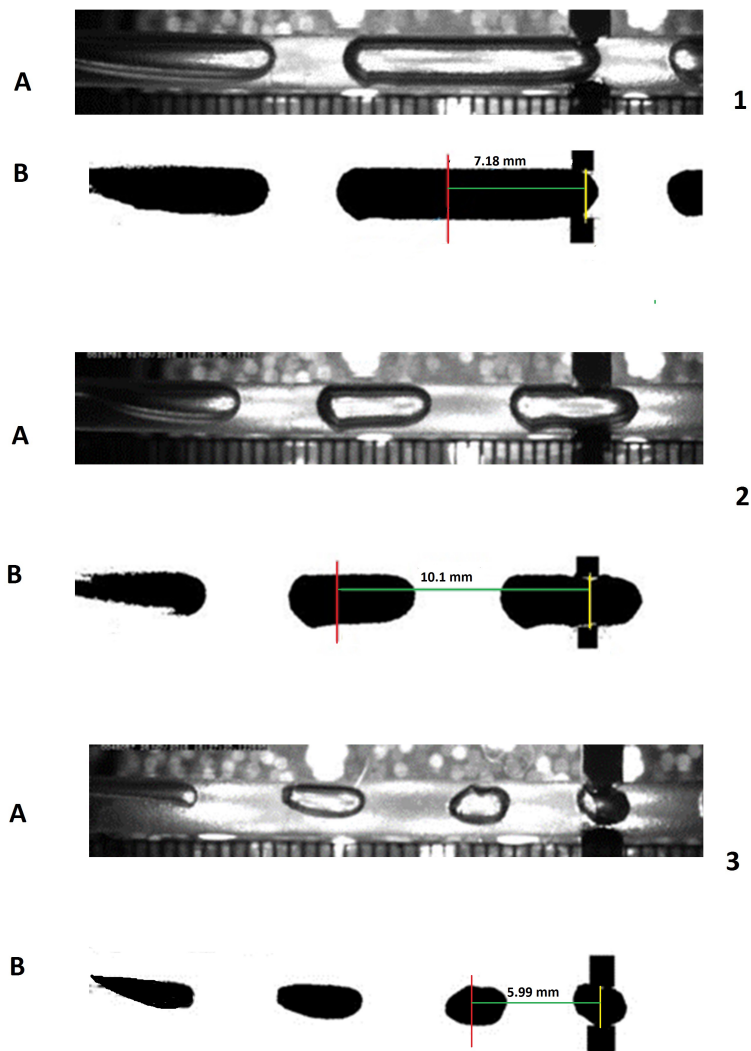


Figure 4.5: Flow conditions and Image measurement locations for case 6 (top), case 5 (middle) and case 1 (bottom).

4.2 Synchronizing Bubble Width and Electrical Response

Direct synchronization between the electrical measurement in LabVIEW and image measurement via the high-speed camera was not achieved with this work. Thus, the electrical response data required synchronization to the image data prior to correlating the voltage response and bubble width. For this purpose, a VBA macro was used to shift the electrical

measurements relative to the image-based width vs time data until the error between the two signals was minimized. An example of the error vs time shift for case 5 is illustrated in Fig. 4.6, with the corresponding phase-matched single appearing in Fig. 4.7.

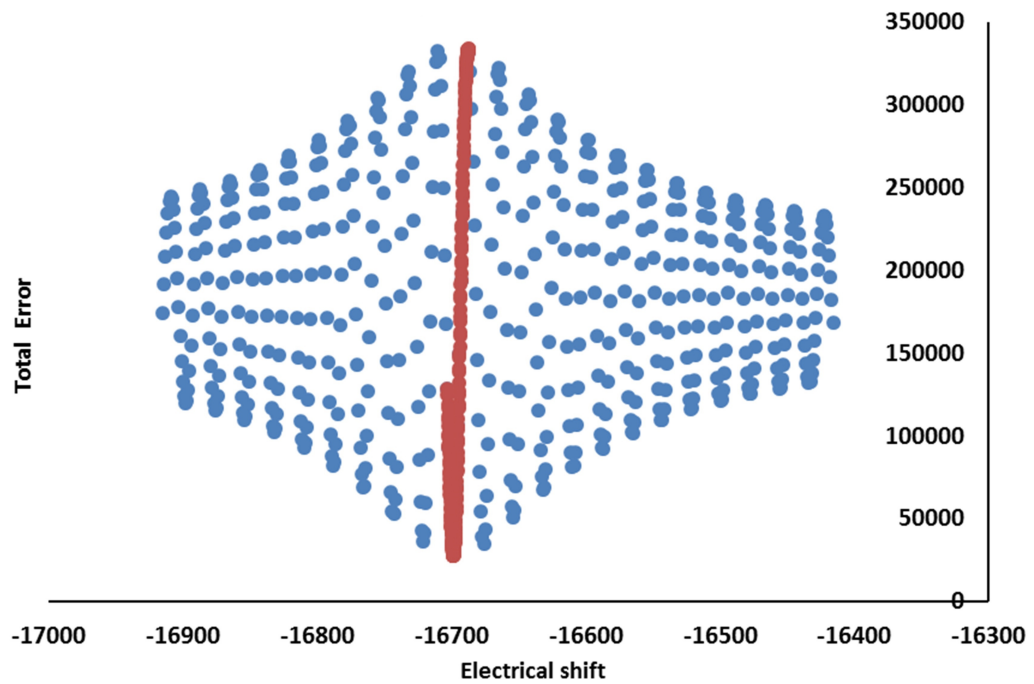


Figure 4.6: Error minimization as a function of the electrical time shift for case (5).

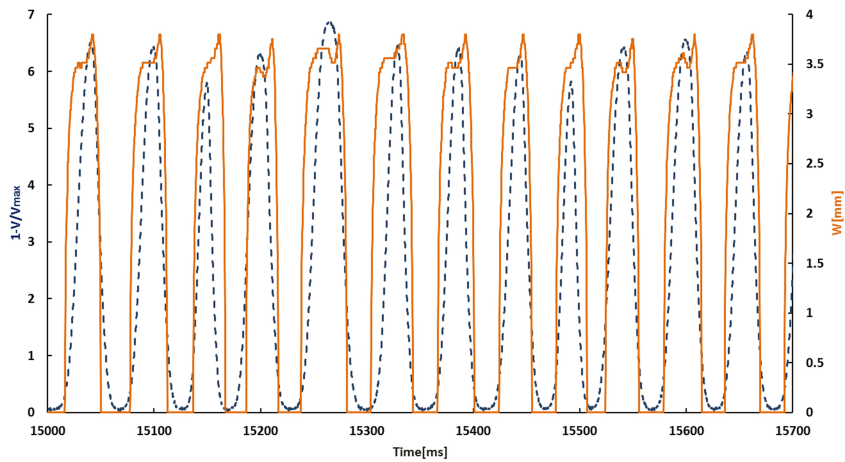


Figure 4.7: Bubble width vs electrical signal at case following alignment (5).

It is important to note that in many of the cases, the image and electrical data collection were active as the first bubbles reached the probe, enabling simpler synchronization simply by aligning the first detected bubble. Other cases required a full time-shift approach when the initial bubbles were not captured as images. Through this synchronization for each experimental test condition, optimum phase matching was achieved between the image data and electrical response. This is required for proper correlation of the electrical response to bubble width.

Chapter 5

RESULTS AND DISCUSSION

5.1 Bubble Velocity From Image Analysis

From the experimental setup, after an image correction has been done, the velocity and gas fraction for different flow rates were calculated. Table 5.1 gives the resulting bubble velocity determined from image analysis, U_{Bimage} , for each of the flow conditions tested, comparing them to the sum of gas and liquid superficial velocities, U_{Bcalc} . Minor variations were attributed to potential variations in the cross-section of the channel and flow rates delivered by the gear pump and mass flow controller, where the image-based measurement is considered to be the most accurate estimate of true bubble velocity at these conditions. It is important to note that bubble velocities in mini-fluidic channels are frequently subject to a capillary number correction due to the presence of a lubricating film surrounding the bubble (Ji et al., 2014). At the channel diameters tested (3.75 mm), the thickness of the lubricating film relative to the channel diameter is negligible, therefore U_{Bimage} is very close in value to the combined superficial velocities of the individual phases.

Table 5.1: Test of a time shift and bubble velocity for distance, gas velocity, and liquid velocity.

Experimental cases	D mm	T_s ms	U_G m/s	U_L m/s	$U_{B\ calc}$ m/s	$U_{B\ image}$ m/s
Case (1)	5.99	7.25	0.147	0.678	0.825	0.826
Case (2)	10.58	28.5	0.074	0.301	0.376	0.371
Case (3)	13.99	32.75	0.148	0.301	0.450	0.427
Case (4)	7.08	13	0.222	0.377	0.599	0.545
Case (5)	10.01	35.75	0.149	0.150	0.30	0.28
Case (6)	7.18	24	0.224	0.075	0.299	0.299
Case (7)	6.4	12.5	0.445	0.075	0.520	0.512

5.2 Bubble Width

Figure 5.1 illustrates the electrical response as bubbles are initially introduced into the flow path. The liquid at rest (point A) has a slightly higher resistance (and lower voltage response) than the liquid under flowing conditions (B and C). There is an initial transition region, as bubbles populate the flow space and the velocity reaches a steady state (point C). At this point the maximum voltage response, V_{max} , was determined for all the flow conditions and compared see Fig. 5.2 to illustrate minimal variation across the conditions tested.

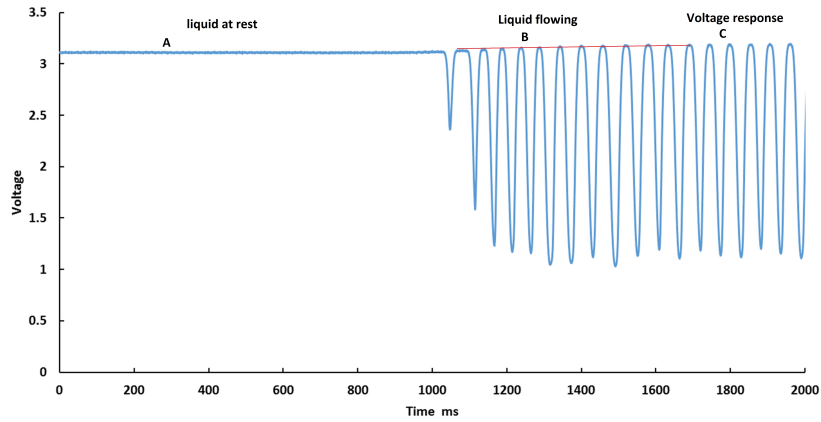


Figure 5.1: Electrical signal response during initial introduction of bubbles for case (5).

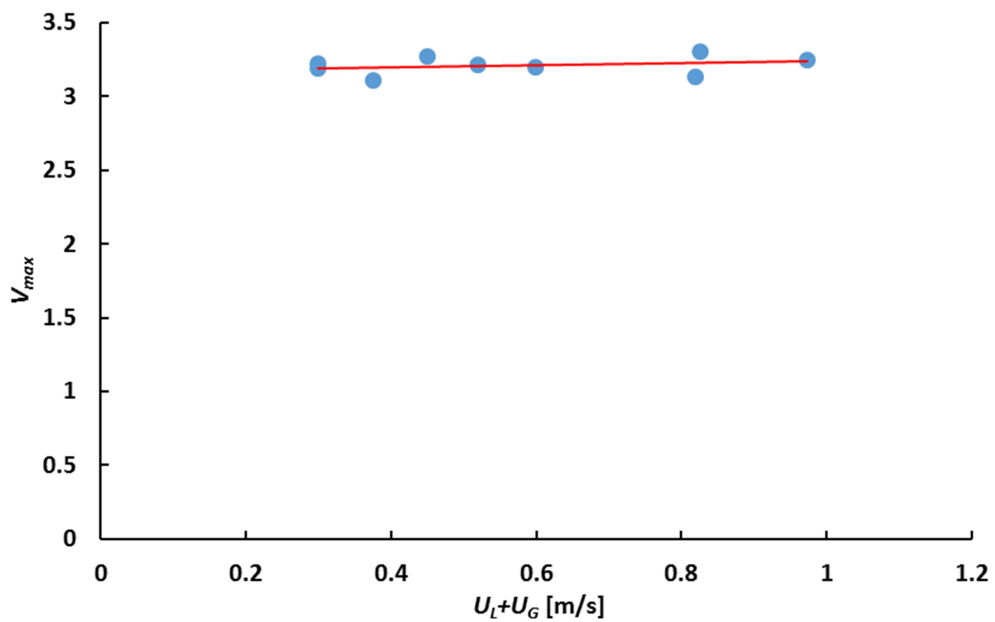


Figure 5.2: V_{max} Determined for each of the flow conditions tested.

The electrical response is an indicator of the total current traveling through the sensor and in-line $200\text{ k}\Omega$ resistor. The electrical resistance model applied in this work uses resistances in series to quantify the impact of flow conditions on electrical resistance, for which the bubble width can be correlated.

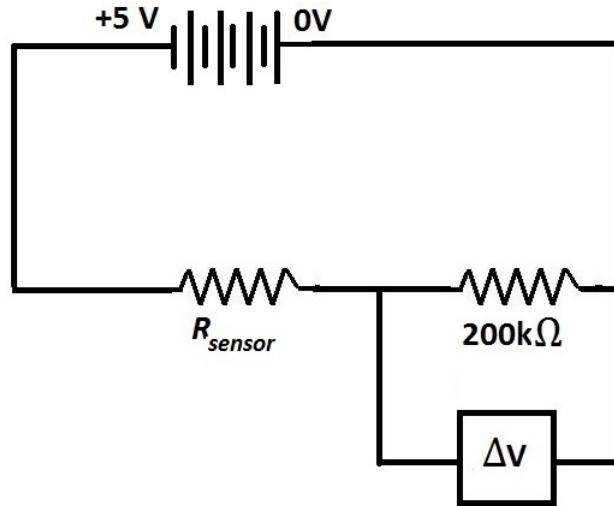


Figure 5.3: Resistance model used within this system.

The current traveling through the sensor and resistor can be approximated as:

$$I[A] = X, W \frac{\Delta V}{200000[\Omega]} \quad (5.1)$$

Based on the total voltage drop of 5 V across the sensor and resistor, the corresponding resistance of the fluid within the sensor can be approximated as:

$$5[V] = IR = \frac{\Delta V}{200000[\Omega]} (R_{sensor} + 2000000[\Omega]) \quad (5.2)$$

Or, rearranging:

$$R_{sensor} = 2000000[\Omega] \left(\frac{5[V]}{\Delta V} - 1 \right) \quad (5.3)$$

Applying Eq. 5.3 to the maximum observed voltage for flow liquid ($\sim 3.2V$) results in an approximate liquid resistance of $112.5 k\Omega$. The conductivity of a fluid, $\kappa [S/m]$, can

be related to its resistance, R_{sensor} , based on the electrical path length, L_{fluid} , and the area available for conduction, A_{fluid} .

$$\kappa = \frac{L_{fluid}}{A_{fluid} R_{sensor}} \quad (5.4)$$

For this specific sensor, the spacing on the electrode was less than the channel diameter, $L_{fluid} \sim 2.88 \text{ mm}$, and using the cross-sectional area of the 14 – gauge wire (2.08 mm^2), the resulting conductivity of the water used was approximately 0.012 S/m . This is consistent with tap water which can vary from 0.005 to 0.05 S/m .

As bubbles are introduced into the flow field, L_{fluid} is increased due to the electrons needing to travel around the interface, while A_{fluid} is decreased due to the bubble occupying some of the cross-section available for conduction Fig. 5.4.

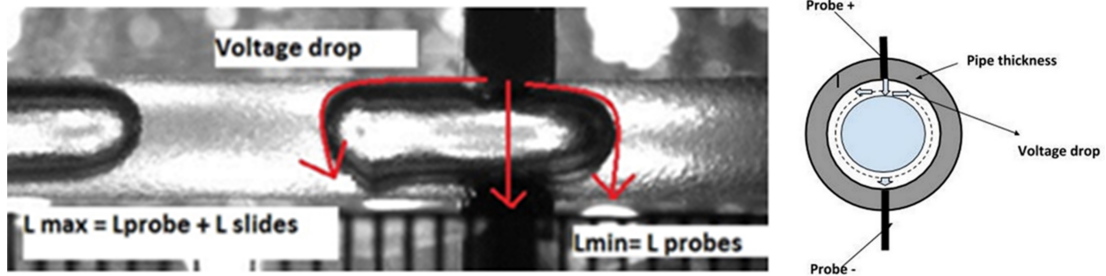


Figure 5.4: Illustration of bubble path length and open area for conduction as bubbles travel through the sensor.

Figure 5.5 illustrates the electrical response of one bubble travelling past the probe at $U_B = 0.28 \text{ m/s}$. In order to correlate the electrical response to the bubble width, a relationship between L_{fluid} , A_{fluid} and bubble width, W , must be derived.

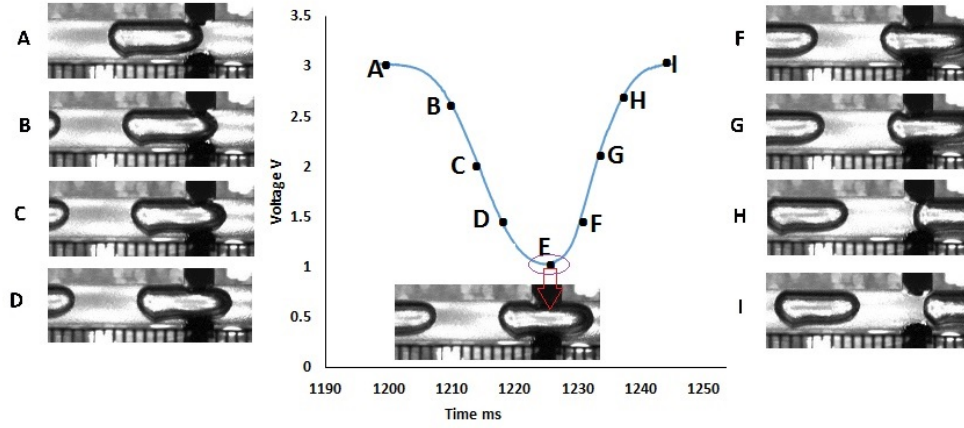


Figure 5.5: Electrical signal response, ΔV , for one bubble traversing the probe.

If it is assumed that the liquid conductivity remains constant within the time frame of the analysis (as applicable for this work, but not necessarily for industrial applications), the measured sensor resistance is directly proportional to the ratio of A_{fluid}/L_{fluid} , where the actual probe response requires empirical calibration, similar to the situation with commercial conductivity sensors. This work focused on determining the proportional relationship between bubble width and measured voltage drop across the $200k\Omega$ resistor. This permitted fitted parameters to be determined, in order to account for the effect of sensor geometry when correlating the bubble width to voltage.

The complete derivation of the relationship between bubble width and voltage response can be found in Appendix A. Two cases were considered, one where the bubble width was relatively small compared to L_{fluid} (i.e., where the effect on the area for conduction was minimal), and the second where the bubble width was comparable to the channel diameter, or extended axially in the channel to create a significant reduction in the area available for electrical conduction. For the first case, the bubble width is proportional to $1 - (\Delta V)/(\Delta V_{max})$. Due to the large size of the bubbles present in most conditions tested

in this work, the approach adopted was that corresponding to the second case. For conditions with large bubbles, it can be shown that:

$$W = \frac{b_1 \max \left[\left(1 - \frac{\Delta V}{\Delta V_{max}} \right) - b_3, 0 \right]}{b_2 + \max \left[\left(1 - \frac{\Delta V}{\Delta V_{max}} \right) - b_3, 0 \right]} \quad (5.5)$$

Where W is predicted bubble width, b_1 , b_2 and b_3 are empirically fitted constants dependent on fluid conductivity, in-line resistor sizing and sensor geometry.

From appendix shown that:

$$b_1 = \frac{D_{channel}}{a_4} = \frac{L_{probe}}{a_2}, \quad (5.6)$$

$$b_2 = \frac{a_3}{a_4(5 + a_3)} \quad (5.7)$$

$$b_3 = \frac{a_3}{(5 + a_3)} \quad (5.8)$$

Where a_1 represent an empirically-derived increase electrical path length as function of the bubble width, and a_2 is an empirical factor effecting the area for conduction depending in channel diameter relative to bubble width. b_1 , b_2 and b_3 are empirically fitting based on the conductivity of the fluids, the sensor geometry and sizing resistor.

Based on the derivation b_1 , b_2 and b_3 are only currently accurate for this specific system if the conductivity of fluids changed we expect to redefine b_2 .

Figure 5.6 provides an example of the bubble width vs $(1 - V/V_{max})$ observed following the synchronization of the image data and electrical measurements.

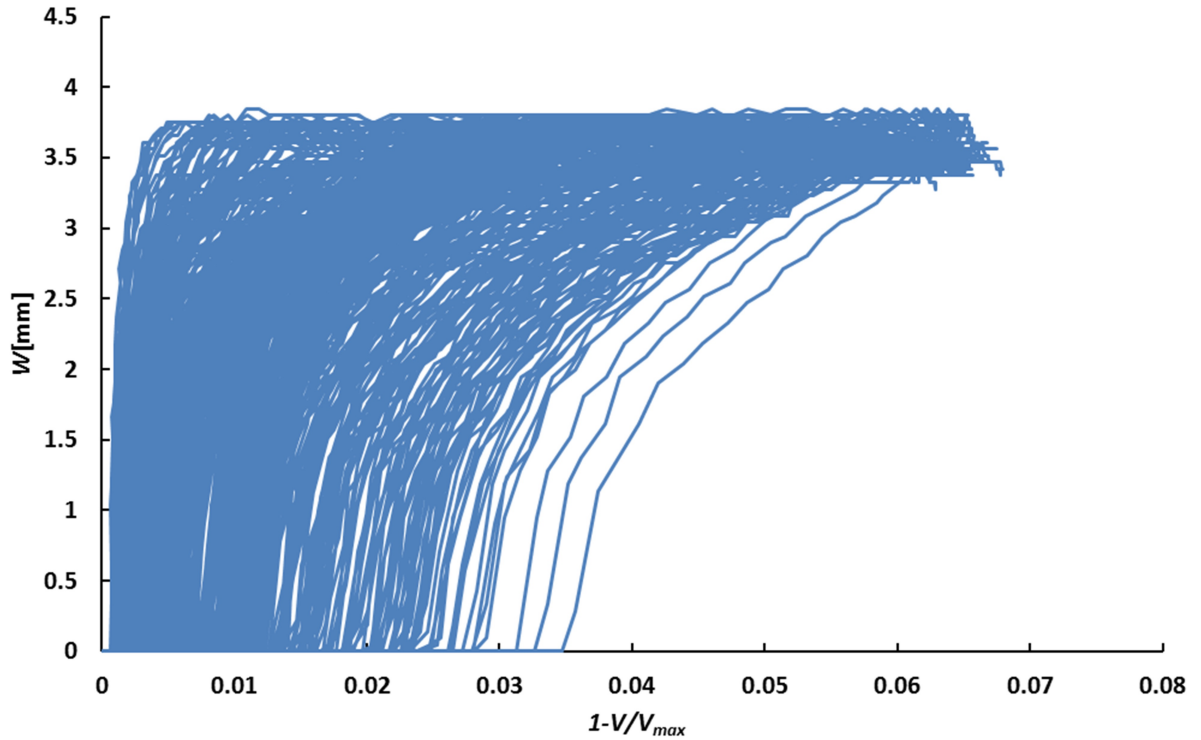


Figure 5.6: Provides an example of the bubble width vs($1 - V/V_{max}$) observed following synchronization of the image data and electrical measurements. .

As each bubble passes through the sensor, the resistance of the fluid varies. The variation in voltage response vs. width observed see Fig. 5.6 is primarily due to the bubble width being derived from a fixed line located at the center of the probe, whereas the electrical response occurs as the bubble travels across the finite flow-path length of the sensor. In other words, the bubble is detected by the electrical probe prior to being detected through integration of the binary images, resulting in leading and trailing “tails” that shift the curves in Fig. 5.6 to the right.

For each of the flow conditions tested, the average bubble width vs electrical response was determined from data recorded for several hundred bubbles. The results are illustrated in Figs. 5.7 and 5.8. Note that most of the variability observed is at smaller bubble widths (i.e., as the bubble enters and leaves the probe), and is primarily due to the leading and trailing

edge effects. As long bubbles travel through the probe, the voltage response becomes non-linear, and the width does not increase proportionally to $1 - V/V_{max}$. This is due to the further reduction in area available for conduction as the gas interface projects into the direction of flow. For example, a spherical bubble provides conduction paths on all sides of the bubble, while an annular bubble shape permits conduction only around the walls of the sensor, not around the leading and trailing edge of the bubble.

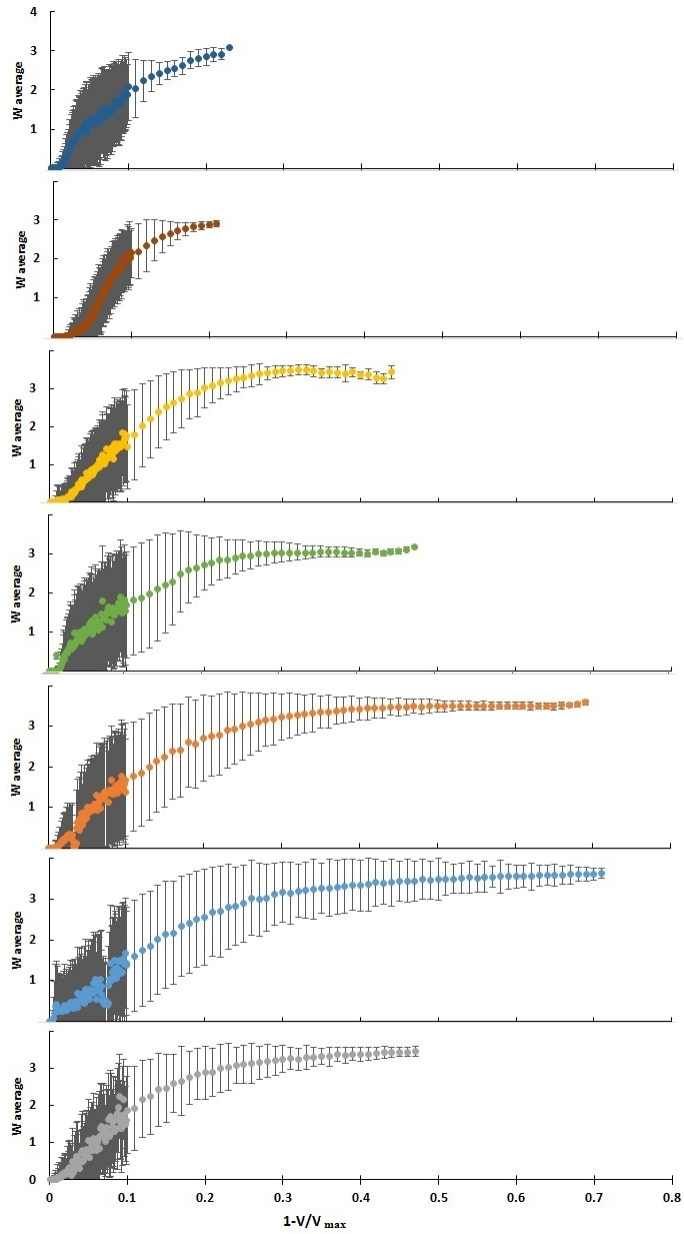


Figure 5.7: Average bubble width vs electrical response for case 1 (top) to case 7 (bottom), and error bars represent a single standard deviation.

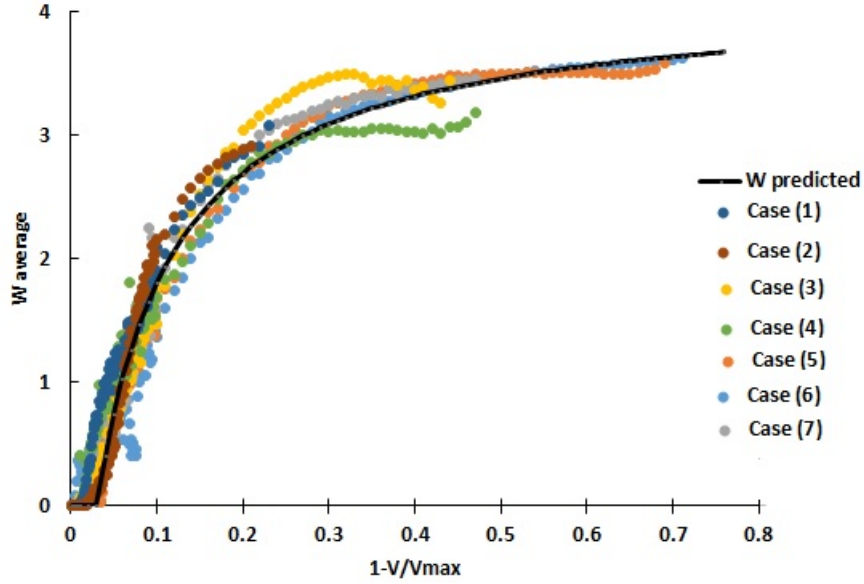


Figure 5.8: Overlay of average bubble width for case 1 (top) to case 7 (bottom).

Figure 5.8 presents an overlay of the bubble width for all experimental conditions, with each line representing the average bubble width for each test. The predicted bubble width is represented by a solid black line, determined through regression of the data to Eq. 5.5. Because the majority of bubble widths intersected the X - axis at $1 - V/V_{max} = 0.03$, b_3 was set to this value. The values of $b_1 = 4.125$ and $b_2 = 0.09$ were subsequently determined to provide an adequate fit for the set of experiments conducted. The resulting bubble width prediction can be expressed as:

$$W = \frac{4.125 \max \left[\left(1 - \frac{\Delta V}{\Delta V_{max}} \right) - 0.03, 0 \right]}{0.09 + \max \left[\left(1 - \frac{\Delta V}{\Delta V_{max}} \right) - 0.03, 0 \right]} \quad (5.9)$$

It should be noted that the derived correlation is specific to this system. b_1 , b_2 and b_3 depend on these terms which mean if the conductivity of fluids is modified this will lead to modify the terms of b_1 , b_2 and b_3 . It may be possible from fundamental derivation of this equation

to account variation conductivity through scale average, however; that has not tested in this work and would have be confirmed.

5.3 Calculated gas hold-up

Gas holdup is the ratio of the gas flow rate to the total flow rate (Tan & Liu, 2016). It is an important parameter for characterizing the velocity or flow field and the turbulence characteristics in the individual phases, as well as the energy dissipation rates (Abdulmouti, 2014). Gas holdup depends upon the average bubble size, the number of bubbles in the pattern, and the calculated bubble velocities.

Gas holdup can be estimated as the integrated fraction of the channel cross-section occupied by the gas over time. For a cylindrical bubble inside a cylindrical pipe, with a constant velocity across the cross-section of the channel, the gas fraction can be approximated as:

$$\alpha_G = \frac{\int_0^{t_{sample}} \frac{\pi W^2}{\pi d^2} dt}{\int_t dt} = \frac{\int_0^{t_{sample}} \left(\frac{W}{d}\right)^2 dt}{t_{sample}} \quad (5.10)$$

Where: α = gas fraction, W = bubble width [mm], and D = channel diameter [3.75 mm]
 t_{sample} = sampling time for the integration [s]

This is generally valid, provided that the shape of the bubbles remains circular in the cross-section of the channel. Through visual observation of the flow patterns illustrated in Table 3.2, it could be seen that cases with lower gas fractions typically exhibited a preferential flow of gas at the top of the channel, due to gravity effects. In the case of completely stratified flow, the fraction of the cross-section occupied by the gas can be more accurately determined from the segment of a circle:

$$\alpha_G = \frac{\int_0^{t_{sample}} \frac{\theta - \sin\theta}{2\pi} dt}{\int_t dt} \sim \frac{\int_0^{t_{sample}} \frac{W}{D} dt}{\int_t dt} \quad (5.11)$$

Where: $\theta = 2 \cos^{-1}(1 - \frac{2W}{D})$. The resulting relationships between W/D and the gas fraction are illustrated in Fig. 5.9. It should be noted that for stratified flow, the gas holdup is roughly linearly dependent on the dimensionless ratio of bubble width to channel diameter, while for the flow of circular gas within a circular channel it is a quadratic function of this ratio.

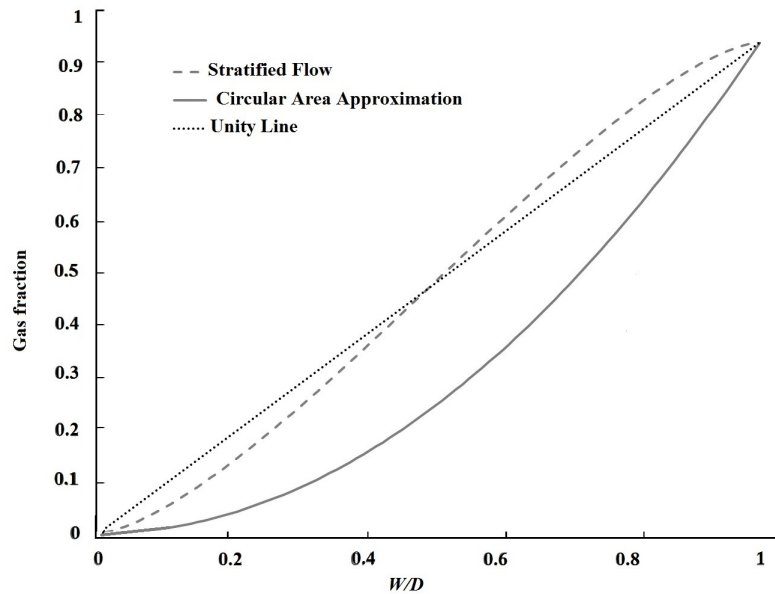


Figure 5.9: Relationship between W/D and gas fraction estimated from Eq.s 5.7 and 5.8 for circular and stratified flow.

The correlation of gas holdup from the predicted bubble width was carried out by using both Eqs. 5.7 and 5.8, recognizing that the two equations represent the extreme limits of the geometric effect of the bubble on the predicted holdup. At high gas fractions, where the bubble shape occupied most of the channel width, there was a minimal difference between the gas fraction predicted through analyses of image data, electrical data and the expected gas holdup based on controlled flow conditions. For a lower gas holdup, the use of a

linear estimate based on W/D (i.e., a simplified model of Eq. 5.8) provided excellent predictions of gas holdup. As a result, the approximated form of Eq. 5.8 was adopted for the experimental analysis of gas holdup in this system.

The integrated gas fraction was determined from both high-speed image data and the voltage-based correlation for bubble width. It is presented in Fig. 5.10 for three cases (1, 7 and 2) at different flow rates and different bubble velocities.

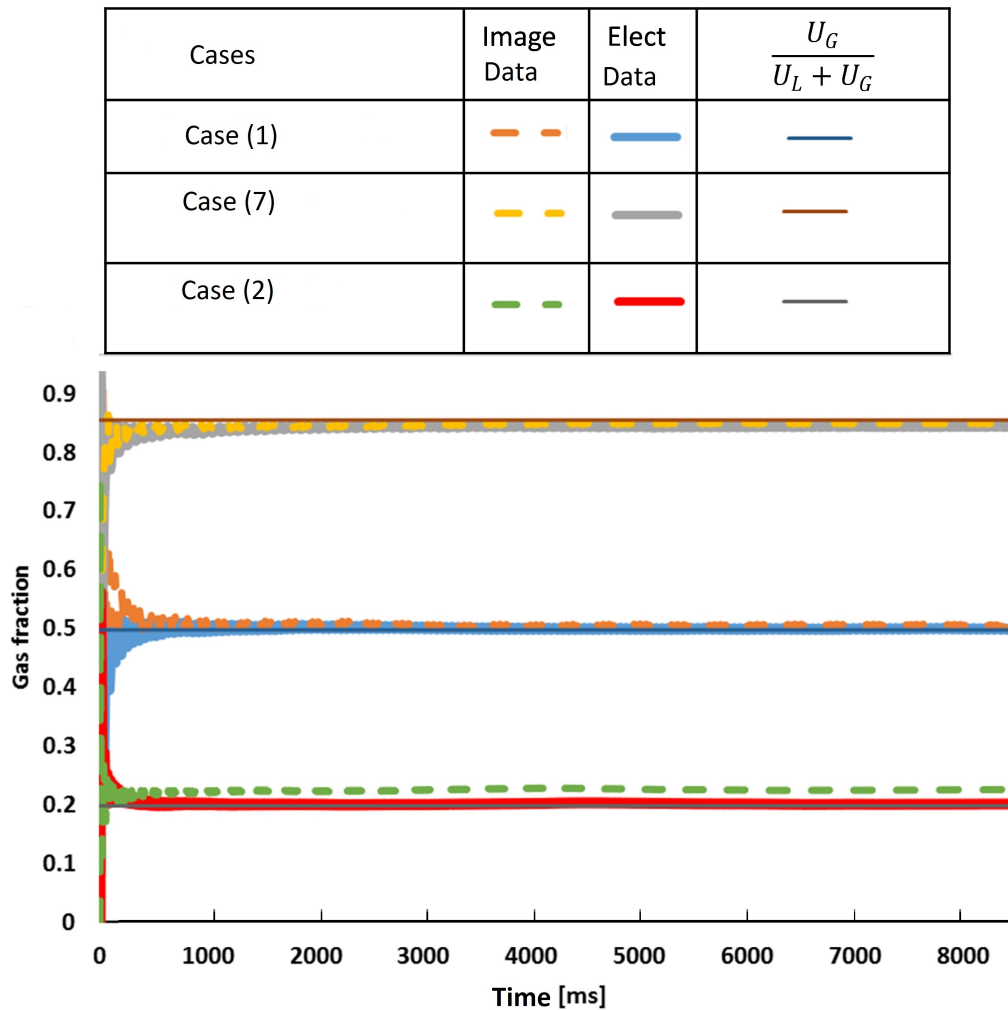


Figure 5.10: Gas fraction for three cases from the image, electrical and flow-based data for increasing values of t_{sample} .

At each flow condition, initial noise in the calculated gas fraction with low sample times was due to the inherent variability of the signals being integrated. As the sample time increased, the predicted gas fractions aligned well with both the image data and the anticipated gas fraction from flow conditions. Fig. 5.11 illustrates the gas fraction calculated from the electrical data for all experimental conditions, while Fig. 5.12 provides a comparison of the calculated gas fraction using $t_{sample} = 10000 [ms]$ to the estimated gas holdup, using $U_G/(U_L + U_G)$ from flow data. Overall, agreement was excellent.

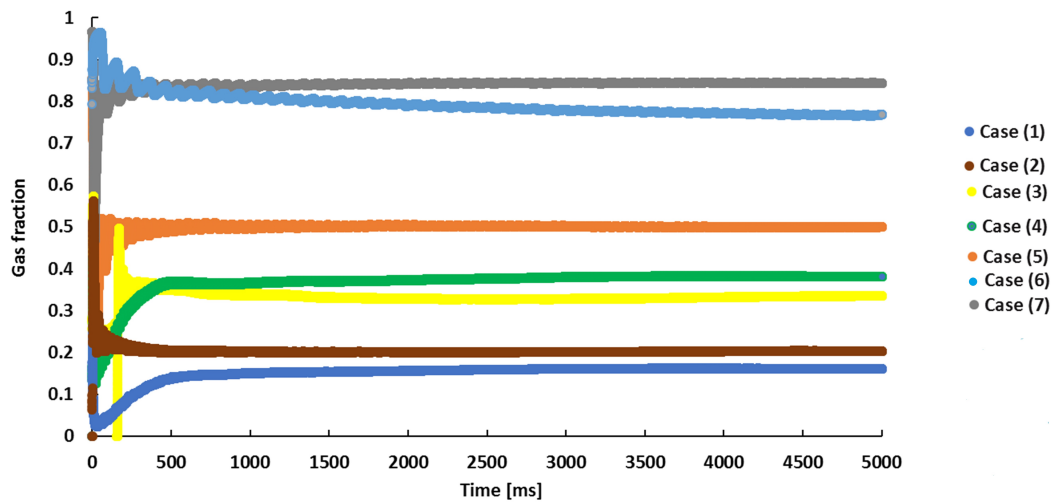


Figure 5.11: Gas fraction from the electrical data for all conditions.

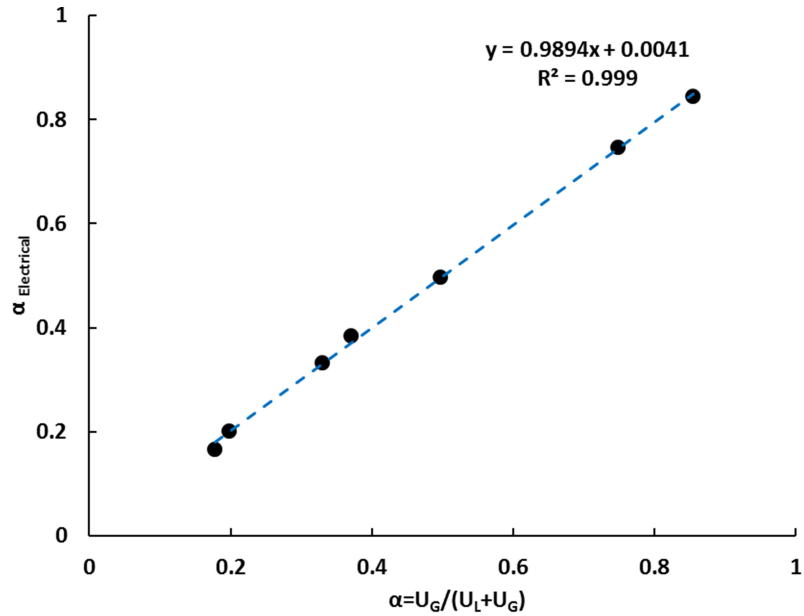


Figure 5.12: Gas fraction from the electrical data vs calculated gas fraction.

5.4 Bubble velocity from single-point measurement

Previously reported conductivity-based methods have relied on measurements at 2 points a known distance apart to determine bubble velocity. This method was applied in Eq. 5.1 for image analysis, yielding excellent prediction results for average bubble velocity for each of the flow conditions tested. A challenge with 2-point measurement is that the first measurement point will affect the flow, introducing changes in the shape of the bubbles or modifying their velocity between the first and second probe locations. Fiber optic probes are commercially available, which enable single-point measurement methods to determine the bubble cord length and rise velocity, based on a pre-calibrated rise time (i.e., the time for the fiber to pierce the gas-liquid film). This work explores the feasibility of performing a similar type of analysis for single-point conductivity measurements in order to approximate bubble velocity within the sensor.

Two approaches were considered: Attempting to correlate the signal rise time to a physical sensing length, from which bubble velocity could be determined; and attempting to correlate the change in measured width vs time to a bubble velocity based on a geometric correlation of bubble shape. The first method relies on the bubbles occupying a significant fraction of the channel geometry, and is challenging even within fiber optic systems, as the fiber must pierce the gas-liquid interface to achieve a binary response (from which the rise time and bubble velocity are calculated). As a result, this work focused on the geometric correlation between the measured rate of change of the bubble width and the correlated velocity for an assumed shape.

A detailed derivation of the correlations is provided in Appendix A. For a hemispherical bubble cap, it can be shown that the velocity is correlated to the measured change in bubble width by:

$$\frac{dX}{dt} = -\frac{1}{2} \frac{W}{W_{max}} \left[1 - \left(\frac{W}{W_{max}} \right)^2 \right]^{-0.5} \frac{dW}{dt} \quad (5.12)$$

When implemented for case 3, the resulting plot of dX/dt vs. W/W_{max} (Fig. 5.13) illustrates that the predicted velocity (0.2 to 0.25 m/s) is significantly less than the experimentally determined velocity of 0.427 m/s for case 3. This discrepancy is probably due to a significant deviation of bubble shape from the assumed hemispherical cap model. A number of alternative geometry correlations were considered, including that of a super-ellipse with multiple adjusted parameters which would enable empirical fitting to the complex shapes of both the leading and trailing edges of the bubble. The challenge with these approaches is that without a physically-based shape correlation, the resulting parameters would have limited applicability outside of this study. Additional work could be done to correlate the shape as a function of flow conditions, but the suggested approach for the future would be to reduce the channel diameter so as to constrain the bubble shape to that of a hemisphere,

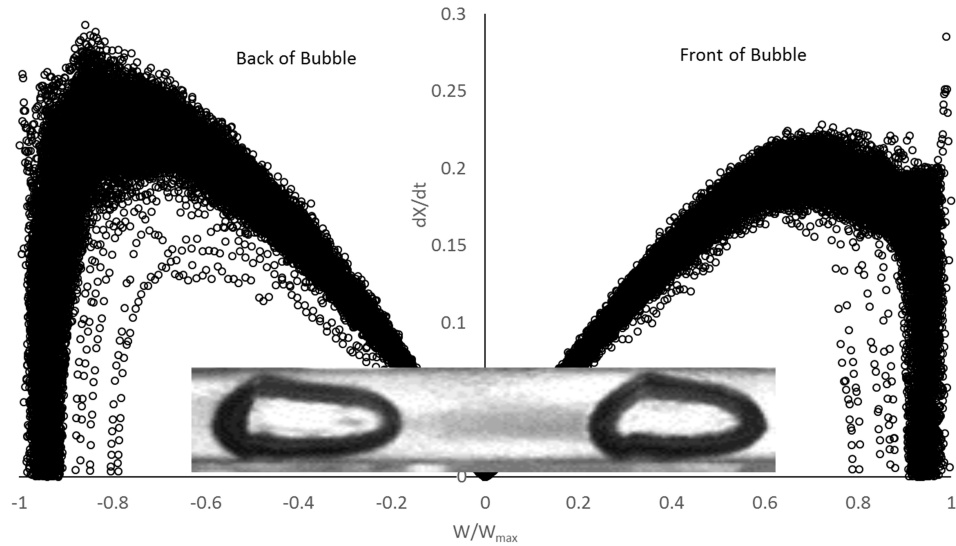


Figure 5.13: Predicted velocity (m/s) vs dimensionless bubble width for case 3.

thus also providing a better correlation between bubble velocity and total fluid velocity, as the bubbles would occupy a significant fraction of the channel width even at the lower range of gas holdups.

Figure 5.13 shows the predicted velocity (m/s) vs. dimensionless bubble width for case 3, with a representative picture of the bubble shape (inset). Note that the flat region near $W/W_{max} = 0.7$ is considered to be the most accurate.

Through analysis of each of the cases tested, it was found that the bubble velocity predicted by Eq. 5.9, when averaged at a value of $W/W_{max} = 0.7$ for both the leading and trailing edges of the bubble, was linearly correlated to the measured bubble velocity determined from image analysis. The significance of $W/W_{max} = 0.7$ is the equivalency of dW/dt and dL/dt at that point for a spherical-capped bubble. This minimizes the potential disparity between the measured and calculated derivatives, and was the region where most of the flattened profiles existed in figures comparable to Fig. 5.12. As an empirical model, specific to this system, the bubble velocity could be approximated from the single-point measurement by the following equation modified from Eq. 5.9:

$$U_B = -1.015 \frac{W}{W_{max}} \left[1 - \left(\frac{W}{W_{max}} \right)^2 \right]^{-0.5} \left| \frac{dW}{dt} \right| \quad (5.13)$$

The resulting equivalency plot is given in Fig. 5.14.

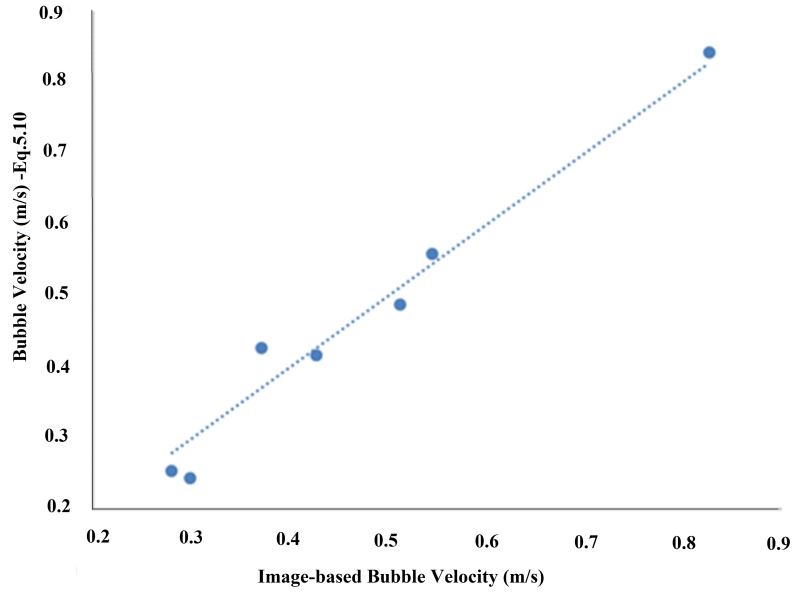


Figure 5.14: Predicted bubble velocity derived from electrical data (Eq. 10) vs. image-based bubble velocities for each of the cases tested.

Chapter 6

CONCLUSION

This thesis investigates the design of a conductive sensor consisting of a voltage source and a measurement device for the determination of the conductivity between two electrical probes inserted into a flow at a spacing of 3.75 mm . One of the most important tasks of this work was to make it possible to investigate the gas holdup and bubble velocity from a single point measurement. Rigorous experimental analyses of the design were carried out to achieve this objective, leading to the following conclusions from this work:

- The methodology used in this work shows potential for estimating gas holdup using a single-point measurement, and reconstructing the bubble shape as a function of time.
- With the single-point measurement method, estimation of the velocity of the bubbles is limited by the large degree of deformation observed in this scale of flow geometry. An empirical correlation was proposed, specific to this system, which appears to provide a rough estimate of bubble velocity, however an extension to new systems is currently limited. It may be possible to improve the control of the shape of the interface and thus the utility of this method, if it is applied in a smaller channel, where the walls would promote the formation of hemi-spherical cap bubbles.

Future work which could assist in the further development of this method includes:

- Correlating the pressure drop through the sensor, and combining it with the phase fraction determined from electrical analysis, to estimate the fluid density for a given fluid pair and the resulting flow rate.
- Reducing the size of the sensor for better control of the bubble shape, to permit a shape-based single-point estimate of bubble velocity.

Bibliography

- Al-Kizwini, M., Wylie, S., Al-Khafaji, D., and Al-Shammai, A. (2013). The monitoring of the two phase flow-annular flow type regime using microwave sensor technique. *Measurement*, 46(1):45–51.
- Aslam, M. Z. and Tang, T. B. (2014). A high resolution capacitive sensing system for the measurement of water content in crude oil. *Sensors*, 14(7):11351–11361.
- Busaidi, K., Bhaskaran, H., et al. (2003). Multiphase flow meters: Experience and assessment in pdo. In *SPE Annual Technical Conference and Exhibition*. Society of Petroleum Engineers.
- Corona, G., Fripp, M., Kalyani, T., Yin, W., et al. (2016). Fluidic diode autonomous inflow control device for heavy oil application. In *SPE Heavy Oil Conference and Exhibition*. Society of Petroleum Engineers.
- Crabtree, R. H. (2009). *The organometallic chemistry of the transition metals*. John Wiley & Sons.
- Da Silva, M., Schleicher, E., and Hampel, U. (2007). Capacitance wire-mesh sensor for fast measurement of phase fraction distributions. *Measurement Science and Technology*, 18(7):2245.
- Demori, M., Ferrari, V., Strazza, D., and Poesio, P. (2010). A capacitive sensor system for the analysis of two-phase flows of oil and conductive water. *Sensors and Actuators A: Physical*, 163(1):172–179.
- Elbuken, C., Glawdel, T., Chan, D., and Ren, C. L. (2011). Detection of microdroplet size and speed using capacitive sensors. *Sensors and Actuators A: Physical*, 171(2):55–62.
- Falcone, G., Hewitt, G., and Alimonti, C. (2009). *Multiphase flow metering: principles and applications*, volume 54. Elsevier.
- Figueiredo, M., Goncalves, J., Nakashima, A., Fileti, A., and Carvalho, R. (2016). The use of an ultrasonic technique and neural networks for identification of the flow pattern and measurement of the gas volume fraction in multiphase flows. *Experimental Thermal and Fluid Science*, 70:29–50.
- Fischer, F., Hoppe, D., Schleicher, E., Mattausch, G., Flaske, H., Bartel, R., and Hampel, U. (2008). An ultra fast electron beam x-ray tomography scanner. *Measurement Science and Technology*, 19(9):094002.

- Fukano, T. (1998). Measurement of time varying thickness of liquid film flowing with high speed gas flow by a constant electric current method (cecm). *Nuclear Engineering and Design*, 184(2):363–377.
- Gang, T., Hu, M., Rong, Q., Qiao, X., Liang, L., Liu, N., Tong, R., Liu, X., and Bian, C. (2016). High-frequency fiber-optic ultrasonic sensor using air micro-bubble for imaging of seismic physical models. *Sensors*, 16(12):2125.
- Gao, Z., Yang, Y., Zhai, L., Jin, N., and Chen, G. (2016). A four-sector conductance method for measuring and characterizing low-velocity oil–water two-phase flows. *IEEE Transactions on Instrumentation and Measurement*, 65(7):1690–1697.
- Goriely, A., Geers, M. G., Holzapfel, G. A., Jayamohan, J., Jérusalem, A., Sivaloganathan, S., Squier, W., van Dommelen, J. A., Waters, S., and Kuhl, E. (2015). Mechanics of the brain: perspectives, challenges, and opportunities. *Biomechanics and modeling in mechanobiology*, 14(5):931–965.
- Hall, A., Griffin, D., and Steven, R. (2007). A discussion on wet gas flow parameter definitions. In *26th International North Sea Flow Meter Workshop, organized by the National Engineering Laboratory, East Kilbride, Scotland, UK*.
- Hampel, U., Otahal, J., Boden, S., Beyer, M., Schleicher, E., Zimmermann, W., and Jicha, M. (2009). Miniature conductivity wire-mesh sensor for gas-liquid two-phase flow measurement. *Flow Measurement and Instrumentation*, 20(1):15–21.
- Hannisdal, A., Westra, R., Akdim, M. R., Bymaster, A., Grave, E., Teng, D. T., et al. (2012). Compact separation technologies and their applicability for subsea field development in deep water. In *Offshore Technology Conference*. Offshore Technology Conference.
- Huh, D., Gu, W., Kamotani, Y., Grotberg, J. B., and Takayama, S. (2005). Microfluidics for flow cytometric analysis of cells and particles. *Physiological measurement*, 26(3):R73.
- Ji, H., Li, H., Huang, Z., Wang, B., and Li, H. (2014). Measurement of gas-liquid two-phase flow in micro-pipes by a capacitance sensor. *Sensors*, 14(12):22431–22446.
- Johansen, G. (2015). Gamma-ray tomography 7. *Industrial Tomography: Systems and Applications*, page 197.
- Kato, A., Onozuka, S., and Kono, F. (2012). Ultrasonic p-wave attenuation measurement for heavy oil. In *SEG Technical Program Expanded Abstracts 2012*, pages 1–5. Society of Exploration Geophysicists.
- Kristiansen, O., Sørensen, Ø., Nilssen, O., et al. (2016). Compact-sep-compact subsea gas-liquid separator for high-pressure wellstream boosting. In *Offshore Technology Conference*. Offshore Technology Conference.
- Leffler, W. L., Pattarozzi, R., and Sterling, G. (2011). *Deepwater petroleum exploration & production: a nontechnical guide*. PennWell Books.

- Lessard, E. (2014). *Measurements in horizontal air-water pipe flows using wire-mesh sensors*. PhD thesis, Université d'Ottawa/University of Ottawa.
- Liang, F., Sun, Y., Yang, G., and Song, L. (2015). Gas-liquid two-phase flow rate measurement with a multi-nozzle sampling method. *Experimental Thermal and Fluid Science*, 68:82–88.
- Lim, L. G., Pao, W. K., Hamid, N. H., and Tang, T. B. (2016). Design of helical capacitance sensor for holdup measurement in two-phase stratified flow: A sinusoidal function approach. *Sensors*, 16(7):1032.
- Liu, H. and Liu, K. T. (2007). Multiphase flow measurement apparatus and method. US Patent 7,311,001.
- Mikkelsen, R., Verbeek, P., Akdim, M. R., et al. (2013). Development of a compact topside processing plant. In *SPE Annual Technical Conference and Exhibition*. Society of Petroleum Engineers.
- Nanes, B. A. (2015). Slide set: Reproducible image analysis and batch processing with imagej. *BioTechniques*, 59(5):269–278.
- Nehring, J., Schuetz, M., Weigel, R., and Kissinger, D. (2014). A microwave permittivity sensing system based on a hybrid heterodyne reflectometer circuit. In *Microwave Conference (EuMC), 2014 44th European*, pages 159–162. IEEE.
- Prescott, N., Mantha, A., Kundu, T., Swenson, J., et al. (2016). Subsea separation-advanced subsea processing with linear pipe separators. In *Offshore Technology Conference*. Offshore Technology Conference.
- Roshani, G., Feghhi, S., Mahmoudi-Aznavah, A., Nazemi, E., and Adineh-Vand, A. (2014). Precise volume fraction prediction in oil-water-gas multiphase flows by means of gamma-ray attenuation and artificial neural networks using one detector. *Measurement*, 51:34–41.
- Roshani, G., Nazemi, E., Feghhi, S., and Setayeshi, S. (2015). Flow regime identification and void fraction prediction in two-phase flows based on gamma ray attenuation. *Measurement*, 62:25–32.
- Schneider, C. A., Rasband, W. S., and Eliceiri, K. W. (2012). Nih image to imagej: 25 years of image analysis. *Nature methods*, 9(7):671.
- Schroder, D. K. (2006). *Semiconductor material and device characterization*. John Wiley & Sons.
- Shamsa, A. and Lines, L. (2015). Effect of oil composition on fluid substitution in heavy oil reservoirs. *Geophysical Prospecting*, 63(2):422–441.

- Shuyu, L. and Shuaijun, W. (2011). Radially composite piezoelectric ceramic tubular transducer in radial vibration. *IEEE transactions on ultrasonics, ferroelectrics, and frequency control*, 58(11).
- Strazza, D., Demori, M., Ferrari, V., and Poesio, P. (2011). Capacitance sensor for hold-up measurement in high-viscous-oil/conductive-water core-annular flows. *Flow Measurement and Instrumentation*, 22(5):360–369.
- Tan, C., Liu, W., and Dong, F. (2016). Characterizing the correlations between local phase fractions of gas–liquid two-phase flow with wire-mesh sensor. *Phil. Trans. R. Soc. A*, 374(2070):20150335.
- Terzic, E., Terzic, J., Nagarajah, R., and Alamgir, M. (2012). Capacitive sensing technology. In *A Neural Network Approach to Fluid Quantity Measurement in Dynamic Environments*, pages 11–37. Springer.
- Uesawa, S.-i., Kaneko, A., and Abe, Y. (2013). Estimation of void fraction in dispersed bubbly flow with a constant electric current method. In *2013 21st International Conference on Nuclear Engineering*, pages V004T09A084–V004T09A084. American Society of Mechanical Engineers.
- Uleh, C. A. (2013). A study of multiphase flow metering at prevailing condition of pressure and temperature.
- Wu, C., Wen, G., Han, L., and Wu, X. (2016). Research on the conductivity-based detection principles of bubbles in two-phase flows and the design of a bubble sensor for cbm wells. *Sensors*, 16(9):1520.
- Wylie, S., Shaw, A., and Al-Shamma'a, A. (2006). Real-time measurements of oil, gas and water contents using an em wave sensor for oil-marine-environment industries. In *Microwave Conference, 2006. 36th European*, pages 451–454. IEEE.

Appendix A

First Appendix

A.1 Bubble Width vs. Voltage Response For Small Bubbles

For small bubbles, the electrical path length is expected to increase based on electrons needing to travel an additional half-bubble circumference due to the bubble being present within the path of conduction.

As a result:

$$L_{fluid} = L_{probe} - W + \frac{\pi W}{2} = L_{probe} - \left(1 - \frac{\pi}{2}\right) W$$

Whereas, L_{fluid} is the electrical path length [mm], L_{probe} the spacing between the probes 2.88 [mm], W is the bubble width [mm],

If the bubbles are sufficiently small, the area for conduction will not be affected significantly. As a result:

$$R_{sensor} = \frac{L_{fluid}}{\kappa A_{fluid}} = \frac{L_{probe} - \left(1 - \frac{\pi}{2}\right) W}{\kappa A_{fluid}} = R_{liquid} + \frac{\left(1 - \frac{\pi}{2}\right) W}{\kappa A_{fluid}}$$

The voltage drop measured for liquid only in the system, ΔV_{max} , can be used as a reference point to determine the relative resistance of the 2-phase solution, and thus W . Given that:

$$R_{liquid} = 200000 [\Omega] \left(\frac{5 [V]}{\Delta V_{max} - 5 [V]} \right)$$

$$R_{liquid} = 200000 [\Omega] \left(\frac{5 [V]}{\Delta V_{max} - 5 [V]} \right)$$

Where as R_{sensor} is total resistances $[\Omega]$, R_{liquid} is the fluid resistance $[\Omega]$ and ΔV_{max} the change in the voltage at liquid $[v]$,

$$200000 [\Omega] \left(\frac{5 [V]}{\Delta V - 5 [V]} \right) = 200000 \left(\frac{5 [V]}{\Delta V_{max} - 5 [V]} \right) + \frac{(1 - \frac{\pi}{2}) W}{\kappa A_{fluid}}$$

$$W = \frac{200000 \kappa A_{fluid}}{(1 - \frac{\pi}{2})} \left(\frac{5}{\Delta V - 5} \frac{5}{\Delta V_{max} - 5} \right)$$

$$W = \frac{100000 \kappa A_{fluid}}{(1 - \frac{\pi}{2})} \left(\frac{1 - \frac{\Delta V}{\Delta V_{max}}}{\left(\frac{\Delta V_{max}}{5} - 1 \right) \left(\frac{5}{\Delta V_{max}} - \frac{\Delta V}{\Delta V_{max}} \right)} \right)$$

Where: A_{fluid} is the area available for conduction $[mm^2]$,

Simplifying this equation would suggest that the Bubble Width is proportional to $1 - \frac{\Delta V}{\Delta V_{max}}$.

Many of the bubbles encountered in this work could not be reasonably considered “small” relative to the width of the channel.

For large bubbles, the exact impact on path length and conduction area is difficult to quantify given the potential impact of bubble shape and elongation in the axial direction. As a result, proportionality constants were used to reflect a reduction in the L/A ratio:

$$L_{fluid} = L_{probe} - W + \frac{\pi W}{2} = L_{probe} - a_1 W$$

$$A_{fluid} = (L_{probe} + a_1 W)$$

Where: a_1 represent the increase electrical path length as function of the bubble width, while a_2 empirical factor effecting the area for conduction depending in channel diameter relative to bubble width. Where a_1 will be negative base on the last definition.

$$A_{fluid} \sim a_2(D_{channel} - W)$$

Where the area available for conduction is assumed to be some form of film between the channel wall and the bubble interface, extending some unknown length in the axial direction, it can be shown that the voltage response expected will have the following form:

$$\Delta V = 5 + 1000000 \left(\frac{\kappa a_2 (D_{channel} - W)}{(L_{probe} - a_1 W)} \right)$$

Similarly, for liquid-only (i.e. $W = 0$):

$$\Delta V_{max} = 5 + 1000000 \left(\frac{\kappa a_2 (D_{channel})}{L_{probe}} \right)$$

For large bubbles, the analysis is initiated by determining the expected relationship between

$1 - \frac{\Delta V}{\Delta V_{max}}$ and the fluid path and fluid area for conduction.

$$\begin{aligned} 1 - \frac{\Delta V}{\Delta V_{max}} &= \frac{5 + 1000000 \left(\frac{\kappa a_2 (D_{channel} - W)}{(L_{probe} - a_1 W)} \right)}{5 + 1000000 \left(\frac{\kappa a_2 (D_{channel})}{L_{probe}} \right)} = \\ &= 1000000 \left(\frac{\kappa a_2 (D_{channel})}{L_{probe}} \right) - 1000000 \left(\frac{\kappa a_2 (D_{channel} - W)}{(L_{probe} - a_1 W)} \right) \end{aligned}$$

A.2 Bubble Width vs. Voltage Response For Small Bubbles

For small bubbles, the electrical path length is expected to increase based on electrons needing to travel an additional half-bubble circumference due to the bubble being present within the path of conduction.

As a result:

$$L_{fluid} = L_{probe} - W + \frac{\pi W}{2} = L_{probe} - \left(1 - \frac{\pi}{2}\right) W$$

Whereas, L_{fluid} is the electrical path length [mm], L_{probe} the spacing between the probes 2.88[mm], W is the bubble width [mm],

If the bubbles are sufficiently small, the area for conduction will not be affected significantly. As a result:

$$R_{sensor} = \frac{L_{fluid}}{\kappa A_{fluid}} = \frac{L_{probe} - \left(1 - \frac{\pi}{2}\right) W}{\kappa A_{fluid}} = R_{liquid} + \frac{\left(1 - \frac{\pi}{2}\right) W}{\kappa A_{fluid}}$$

The voltage drop measured for liquid only in the system, ΔV_{max} , can be used as a reference point to determine the relative resistance of the 2-phase solution, and thus W . Given that:

$$R_{liquid} = 200000 [\Omega] \left(\frac{5 [V]}{\Delta V_{max} - 5 [V]} \right)$$

$$R_{liquid} = 200000 [\Omega] \left(\frac{5 [V]}{\Delta V_{max} - 5 [V]} \right)$$

Whereas, R_{sensor} is total resistances [Ω], R_{liquid} is the fluid resistance [Ω] and ΔV_{max} the change in the voltage at liquid [v],

$$200000 [\Omega] \left(\frac{5 [V]}{\Delta V - 5 [V]} \right) = 200000 \left(\frac{5 [V]}{\Delta V_{max} - 5 [V]} \right) + \frac{(1 - \frac{\pi}{2}) W}{\kappa A_{fluid}}$$

$$W = \frac{200000 \kappa A_{fluid}}{(1 - \frac{\pi}{2})} \left(\frac{5}{\Delta V - 5} \frac{5}{\Delta V_{max} - 5} \right)$$

$$W = \frac{100000 \kappa A_{fluid}}{(1 - \frac{\pi}{2})} \left(\frac{1 - \frac{\Delta V}{\Delta V_{max}}}{\left(\frac{\Delta V_{max}}{5} - 1 \right) \left(\frac{5}{\Delta V_{max}} - \frac{\Delta V}{\Delta V_{max}} \right)} \right)$$

Where: A_{fluid} is the area available for conduction [mm^2],

Simplifying this equation would suggest that the Bubble Width is proportional to $1 - \frac{\Delta V}{\Delta V_{max}}$.

Many of the bubbles encountered in this work could not be reasonably considered “small” relative to the width of the channel.

For large bubbles, the exact impact on path length and conduction area is difficult to quantify given the potential impact of bubble shape and elongation in the axial direction. As a result, proportionality constants were used to reflect a reduction in the L/A ratio:

$$L_{fluid} = L_{probe} - W + \frac{\pi W}{2} = L_{probe} - a_1 W$$

$$A_{fluid} = (L_{probe} + a_1 W)$$

Where a_1 represent the increase electrical path length as function of the bubble width, while a_2 empirical factor effecting the area for conduction depending in channel diameter relative to bubble width. Where a_1 will be negative base on the last definition.

$$A_{fluid} \sim a_2 (D_{channel} - W)$$

Where the area available for conduction is assumed to be some form of film between the channel wall and the bubble interface, extending some unknown length in the axial direction, it can be shown that the voltage response expected will have the following form:

$$\Delta V = 5 + 1000000 \left(\frac{\kappa a_2 (D_{channel} - W)}{(L_{probe} - a_1 W)} \right)$$

Similarly, for liquid-only (i.e. $W = 0$):

$$\Delta V_{max} = 5 + 1000000 \left(\frac{\kappa a_2 (D_{channel})}{L_{probe}} \right)$$

For large bubbles, the analysis is initiated by determining the expected relationship between $1 - \frac{\Delta V}{\Delta V_{max}}$ and the fluid path and fluid area for conduction:

$$\begin{aligned} 1 - \frac{\Delta V}{\Delta V_{max}} &= \frac{5 + 1000000 \left(\frac{\kappa a_2 (D_{channel} - W)}{(L_{probe} - a_1 W)} \right)}{5 + 1000000 \left(\frac{\kappa a_2 (D_{channel})}{L_{probe}} \right)} = \\ &= 1000000 \left(\frac{\kappa a_2 (D_{channel})}{L_{probe}} \right) - 1000000 \left(\frac{\kappa a_2 (D_{channel} - W)}{(L_{probe} - a_1 W)} \right) \\ W \propto \left[\frac{1 - V}{V_{liq}} \right] 1 - \frac{V}{V_{liq}} &= \frac{IR_{liq} - IR_{2ph}}{IR_{liq}} = \frac{a_1 KL - a_2 KL \frac{L(L-W)}{L + (\frac{\pi}{2} - 1)W}}{a_1 KL} \end{aligned}$$

$$\begin{aligned} 1 - \frac{\Delta V}{\Delta V_{max}} &= \frac{5 + 1000000 \left(\frac{\kappa a_2 (D_{channel} - W)}{(L_{probe} - a_1 W)} \right)}{5 + 1000000 \left(\frac{\kappa a_2 (D_{channel})}{L_{probe}} \right)} = \\ &= 1000000 \left(\frac{\kappa a_2 (D_{channel})}{L_{probe}} \right) - 1000000 \left(\frac{\kappa a_2 (D_{channel} - W)}{(L_{probe} - a_1 W)} \right) \end{aligned}$$

By defining a constant, $a_3 = \frac{1000000(\kappa a_2 D_{channel})}{L_{probe}}$, this equation can be shown as:

$$1 - \frac{\Delta V}{\Delta V_{max}} = \frac{a_3 - a_3 \left(\frac{(1 - \frac{W}{D_{channel}})}{(1 - a_1 \frac{W}{L_{probe}})} \right)}{5 + a_3}$$

This equation is subsequently rearranged for W :

$$\left[\left(1 - \frac{\Delta V}{\Delta V_{max}} \right) \left(\frac{5+a_3}{a_3} \right) \right] \left(1 - a_1 \frac{W}{L_{probe}} \right) = \left(1 - \frac{W}{D_{channel}} \right)$$

$$\left[\left(1 - \frac{\Delta V}{\Delta V_{max}} \right) \left(\frac{5+a_3}{a_3} \right) \right] \left(a_1 \frac{W}{L_{probe}} \right) = \left(1 - \frac{W}{D_{channel}} \right) - 1$$

Defining $a_4 = \frac{a_2 D_{channel}}{L_{probe}}$

$$\left[\left(1 - \frac{\Delta V}{\Delta V_{max}} \right) \left(\frac{5+a_3}{a_3} \right) \right] \left(a_4 \frac{W}{L_{probe}} \right) = \left(1 - \frac{W}{D_{channel}} \right) - 1$$

Rearranging for $W/D_{channel}$

$$\frac{W}{D_{channel}} = \frac{\frac{(5+a_3)}{a_3} \left(1 - \frac{\Delta V}{\Delta V_{max}} \right)}{1 + a_4 \left[\frac{(5+a_3)}{a_3} \left(1 - \frac{\Delta V}{\Delta V_{max}} \right) - 1 \right]}$$

$$\frac{W}{D_{channel}} = \frac{\frac{1}{a_4} \left(1 - \frac{\Delta V}{\Delta V_{max}} \right)}{\frac{a_3}{a_4(5+a_3)} \left[\left(1 - \frac{\Delta V}{\Delta V_{max}} \right) - \frac{a_3}{(5+a_3)} \right]}$$

Given that a_3 and a_4 are empirical constants, the expression can be further simplified by defining:

$$b_1 = \frac{D_{channel}}{a_4} = \frac{L_{probe}}{a_2},$$

$$b_2 = \frac{a_3}{a_4(5+a_3)}$$

and

$$b_3 = \frac{a_3}{(5 + a_3)}$$

such that:

$$W = \frac{b_1 \left(1 - \frac{\Delta V}{\Delta V_{max}} \right)}{\left(b_2 + \left(1 - \frac{\Delta V}{\Delta V_{max}} \right) - b_3 \right)}$$

Note that $D_{channel}$ has been incorporated into the b_1 constant. It was noted in experiments that the finite width of the electrical probe resulted in a slight shift in low voltage values, where $\left(1 - \frac{\Delta V}{\Delta V_{max}} \right) = 0.03$ appeared even when no bubbles were present. As a result, the derived expression for W was modified slightly to the form of:

$$W = \frac{b_1 \max \left[\left(1 - \frac{\Delta V}{\Delta V_{max}} \right) - b_3, 0.03 \right]}{b_2 + \max \left[\left(1 - \frac{\Delta V}{\Delta V_{max}} \right) - b_3, 0.03 \right]}$$

Where: b_3 was set equal to 0.03 and a max function was introduced to limit width predictions to measurements where $\left(1 - \frac{\Delta V}{\Delta V_{max}} \right) > 0.03$

A.3 Bubble Velocity

Where the electrical measurements provide a method for estimating the bubble width, W , the bubble velocity can be estimated if the bubble passing through the sensor has a consistent shape. For example, given the equation for a hemi-spherical interface having a radius of $0.5W_{max}$ in an X, W coordinate system:

$$\left(\frac{X}{0.5W_{max}} \right)^2 + \left(\frac{W}{W_{max}} \right)^2 = 1$$

The velocity, dX/dt , can be estimated by taking the partial derivative with respect to time:

$$2 \left(\frac{2X}{W_{max}} \right) \frac{2}{W_{max}} \frac{dX}{dt} + \left(\frac{W}{W_{max}} \right) \frac{2}{W_{max}} \frac{dW}{dt} = 0$$

$$\frac{8X}{W_{max}^2} \frac{dX}{dt} = - \frac{2W}{W_{max}^2} \frac{dW}{dt}$$

$$\frac{dX}{dt} = - \frac{1}{4} \frac{W}{X} \frac{dW}{dt}$$

Rearranging the equation of the hemi-spherical curve for X and substituting it into the derivative expression yields:

$$X = \frac{W_{max}}{2} \left[1 - \left(\frac{W}{W_{max}} \right)^2 \right]^{0.5}$$

$$\frac{dX}{dt} = \frac{1}{2} \frac{W}{W_{max}} \left[1 - \left(\frac{W}{W_{max}} \right)^2 \right]^{0.5} \frac{dW}{dt}$$

$$W_{\infty} \left[\frac{1-V}{V_{liq}} \right] 1 - \frac{V}{V_{liq}} = \frac{IR_{liq} - IR_{2ph}}{IR_{liq}} = \frac{a_1 KL - a_2 KL \frac{L(L-W)}{L+(\frac{\pi}{2}-1)W}}{a_1 KL}$$

$$\begin{aligned} 1 - \frac{\Delta V}{\Delta V_{max}} &= \frac{5 + 1000000 \left(\frac{\kappa a_2 (D_{channel} - W)}{(L_{probe} - a_1 W)} \right)}{5 + 1000000 \left(\frac{\kappa a_2 (D_{channel})}{L_{probe}} \right)} = \\ &= 1000000 \left(\frac{\kappa a_2 (D_{channel})}{L_{probe}} \right) - 1000000 \left(\frac{\kappa a_2 (D_{channel} - W)}{(L_{probe} - a_1 W)} \right) \end{aligned}$$

By defining a constant, $a_3 = \frac{1000000(\kappa a_2 D_{channel})}{L_{probe}}$ this equation can be shown as:

$$1 - \frac{\Delta V}{\Delta V_{max}} = \frac{a_3 - a_3 \left(\frac{(1 - \frac{W}{D_{channel}})}{(1 - a_1 \frac{W}{L_{probe}})} \right)}{5 + a_3}$$

This equation is subsequently rearranged for W :

$$\left[\left(1 - \frac{\Delta V}{\Delta V_{max}} \right) \left(\frac{5+a_3}{a_3} \right) \right] \left(1 - a_1 \frac{W}{L_{probe}} \right) = \left(1 - \frac{W}{D_{channel}} \right)$$

$$\left[\left(1 - \frac{\Delta V}{\Delta V_{max}} \right) \left(\frac{5+a_3}{a_3} \right) \right] - \left[\left(1 - \frac{\Delta V}{\Delta V_{max}} \right) \left(\frac{5+a_3}{a_3} \right) - 1 \right] \left(a_1 \frac{W}{L_{probe}} \right) = \left(1 - \frac{W}{D_{channel}} \right)$$

Defining $a_4 = \frac{a_2 D_{channel}}{L_{probe}}$

$$\left[\left(1 - \frac{\Delta V}{\Delta V_{max}} \right) \left(\frac{5+a_3}{a_3} \right) \right] - \left[\left(1 - \frac{\Delta V}{\Delta V_{max}} \right) \left(\frac{5+a_3}{a_3} \right) - 1 \right] \left(a_4 \frac{W}{L_{probe}} \right) = \left(1 - \frac{W}{D_{channel}} \right)$$

Rearranging for $W/D_{channel}$

$$\frac{W}{D_{channel}} = \frac{\frac{(5+a_3)}{a_3} \left(1 - \frac{\Delta V}{\Delta V_{max}} \right)}{1 + a_4 \left[\frac{(5+a_3)}{a_3} \left(1 - \frac{\Delta V}{\Delta V_{max}} \right) - 1 \right]}$$

$$\frac{W}{D_{channel}} = \frac{\frac{1}{a_4} \left(1 - \frac{\Delta V}{\Delta V_{max}} \right)}{\frac{a_3}{a_4(5+a_3)} \left[\left(1 - \frac{\Delta V}{\Delta V_{max}} \right) - \frac{a_3}{(5+a_3)} \right]}$$

Given that a_3 and a_4 are empirical constants, the expression can be further simplified by defining:

$$b_1 = \frac{D_{channel}}{a_4} = \frac{L_{probe}}{a_2},$$

$$b_2 = \frac{a_3}{a_4(5+a_3)}$$

and

$$b_3 = \frac{a_3}{(5 + a_3)}$$

such that:

$$W = \frac{b_1 \left(\left[1 - \frac{\Delta V}{\Delta V_{max}} \right] \right)}{\left(b_2 + \left(\left[1 - \frac{\Delta V}{\Delta V_{max}} \right] - b_3 \right) \right)}$$

Note that $D_{channel}$ has been incorporated into the b_1 constant. It was noted in experiments that the finite width of the electrical probe resulted in a slight shift in low voltage values, where $\left(1 - \frac{\Delta V}{\Delta V_{max}} \right) = 0.03$ appeared even when no bubbles were present. As a result, the derived expression for W was modified slightly to the form of:

$$W = \frac{b_1 \max \left[\left(1 - \frac{\Delta V}{\Delta V_{max}} \right) - b_3, 0.03 \right]}{b_2 + \max \left[\left(1 - \frac{\Delta V}{\Delta V_{max}} \right) - b_3, 0.03 \right]}$$

Where: b_3 was set equal to 0.03 and a max function was introduced to limit width predictions to measurements where $\left(1 - \frac{\Delta V}{\Delta V_{max}} \right) > 0.03$

A.4 Bubble Velocity

Where the electrical measurements provide a method for estimating the bubble width, W , the bubble velocity can be estimated if the bubble passing through the sensor has a consistent shape. For example, given the equation for a hemi-spherical interface having a radius of $0.5W_{max}$ in an X, W coordinate system:

$$\left(\frac{X}{0.5W_{max}} \right)^2 + \left(\frac{W}{W_{max}} \right)^2 = 1$$

The velocity, dX/dt , can be estimated by taking the partial derivative with respect to time:

$$2 \left(\frac{2X}{W_{max}} \right) \frac{2}{W_{max}} \frac{dX}{dt} + \left(\frac{W}{W_{max}} \right) \frac{2}{W_{max}} \frac{dW}{dt} = 0$$

$$\frac{8X}{W_{max}^2} \frac{dX}{dt} = - \frac{2W}{W_{max}^2} \frac{dW}{dt}$$

$$\frac{dX}{dt} = - \frac{1}{4} \frac{W}{X} \frac{dW}{dt}$$

Rearranging the equation of the hemi-spherical curve for X and substituting it into the derivative expression yields:

$$X = \frac{W_{max}}{2} \left[1 - \left(\frac{W}{W_{max}} \right)^2 \right]^{0.5}$$

$$\frac{dX}{dt} = \frac{1}{2} \frac{W}{W_{max}} \left[1 - \left(\frac{W}{W_{max}} \right)^2 \right]^{0.5} \frac{dW}{dt}$$